Open Research Online

Optically detected galaxy cluster candidates in the *AKARI* North Ecliptic Pole field based on photometric redshift from the Subaru Hyper Suprime-Cam

Journal Item

For guidance on citations see FAQs.

Version: Version of Record

Link(s) to article on publisher's website:
http://dx.doi.org/doi:10.1093/mnras/stab2128

Optically detected galaxy cluster candidates in the *AKARI* North Ecliptic Pole field based on photometric redshift from the Subaru Hyper Suprime-Cam

Ting-Chi Huang [1,2]★ Hideo Matsuhara,[1,2] Tomotsugu Goto,[3] Daryl Joe D. Santos,[3] Simon C.-C. Ho [3] Seong Jin Kim [3] Tetsuya Hashimoto [3,4,26] Hiroyuki Ikeda,[5,6] Nagisa Oi [7] Matthew A. Malkan,[8] William J. Pearson [9] Agnieszka Pollo,[9,10] Stephen Serjeant [11] Hyunjin Shim,[12] Takamitsu Miyaji [13,14] Ho Seong Hwang [15,27] Anna Durkalec,[9] Artem Poliszczuk,[9] Thomas R. Greve,[16,17,18] Chris Pearson [11,19,20] Yoshiki Toba [21,22,23] Dongseob Lee,[12] Helen K. Kim,[8] Sune Toft,[17,24] Woong-Seob Jeong[25] and Umi Enokidani[1,2]

Affiliations are listed at the end of the paper

ABSTRACT

Galaxy clusters provide an excellent probe in various research fields in astrophysics and cosmology. However, the number of galaxy clusters detected so far in the *AKARI* North Ecliptic Pole (NEP) field is limited. In this work, we provide galaxy cluster candidates in the *AKARI* NEP field with the minimum requisites based only on the coordinates and photometric redshift (photo-z) of galaxies. We used galaxies detected in five optical bands (g, r, i, z, and Y) by the Subaru Hyper Suprime-Cam (HSC), with additional data from the u band obtained from the Canada-France-Hawaii Telescope (CFHT) MegaPrime/MegaCam, and from the IRAC1 and IRAC2 bands from the *Spitzer* space telescope for photo-z estimation. We calculated the local density around every galaxy using the 10th-nearest neighbourhood. Cluster candidates were determined by applying the friends-of-friends algorithm to over-densities. A total of 88 cluster candidates containing 4390 member galaxies below redshift 1.1 in 5.4 deg^2 were identified. The reliability of our method was examined through false-detection tests, redshift-uncertainty tests, and applications on the Cosmic Evolution Survey (COSMOS) data, giving false-detection rates of 0.01 to 0.05 and a recovery rate of 0.9 at high richness. Three X-ray clusters previously observed by *ROSAT* and *Chandra* were recovered. The cluster galaxies show a higher stellar mass and lower star formation rate compared with the field galaxies in two-sample Z-tests. These cluster candidates are useful for environmental studies of galaxy evolution and future astronomical surveys in the NEP, where *AKARI* has performed unique nine-band mid-infrared photometry for tens of thousands of galaxies.

Key words: methods: data analysis – galaxies: clusters: general – galaxies: distance and redshifts – galaxies: evolution – galaxies: groups: general.

1 INTRODUCTION

Clusters of galaxies are very important astronomical objects, having a wide variety of uses in many research fields in both astrophysics and cosmology. For example, because of their high density, clusters of galaxies are good laboratories for studying the environmental effect on galaxy evolution (e.g. Goto et al. 2003; Park & Hwang 2009; Vulcani et al. 2010; Hwang, Park & Choi 2012). In addition, clusters of galaxies, as massively bound systems in the large-scale structure of the Universe, can provide measurement of the standard ruler in baryon acoustic oscillations for cosmological studies (e.g. Hong et al. 2012; Hong, Han & Wen 2016). Clusters of galaxies are also frequently used as gravitational lenses to observe faint or high-redshift galaxies (e.g. Coe et al. 2013).

There are many approaches to detecting galaxy clusters, using their various characteristics at different wavelengths. The intracluster medium consists of hot gas at a temperature of more than 10^8 K, owing to inefficient cooling by the bremsstrahlung process, which emits radiation in the X-ray. Therefore, identifying galaxy clusters from X-ray surveys is relatively straightforward (e.g. Böehringer et al. 2001; Takey, Schwope & Lamer 2011). Furthermore, high-energy electrons interact with the cosmic microwave background (CMB) photons through inverse Compton scattering, and distort the CMB spectrum, a phenomenon known as the Sunyaev–Zeldovich (SZ) effect (Sunyaev & Zeldovich 1980). Thus, galaxy clusters are also frequently detected at millimetre wavelength by either ground-based (e.g. Staniszewski et al. 2009; Bleem et al. 2015; Hilton et al. 2020) or space-based (e.g. Planck Collaboration XXIX 2014; Planck Collaboration XXVII 2016) telescopes. Currently, more and more cluster-finding algorithms using optical photometric or spectroscopic data of galaxies are being developed. These methods generally utilize

★ E-mail: s104022505@m104.nthu.edu.tw

the colour of the cluster red sequence (e.g. Muzzin et al. 2013; Rykoff et al. 2014; Oguri et al. 2018), or the density enhancement associated with the galaxy redshift (e.g. Wen, Han & Liu 2012; Tempel et al. 2014; Hung et al. 2020), or both (e.g. Goto et al. 2002, 2008). All of these approaches have their advantages and disadvantages. Using optical photometric data allows us to find as many galaxy clusters as possible, because they are generally observed by large-area deep surveys, providing numerous samples of galaxies. In this work, we used optical photometric data from the Subaru Hyper Suprime-Cam (HSC) to search for clusters in the *AKARI* North Ecliptic Pole (NEP) field.

AKARI is an infrared space telescope launched by the Japan Aerospace Exploration Agency (JAXA) in 2006 (Murakami et al. 2007). It carried out a 5.4-deg^2 survey at the NEP (Kim et al. 2012) using its Infrared Camera (IRC; Onaka et al. 2007), which is equipped with nine filters in the mid-infrared ($N2$, $N3$, $N4$, $S7$, $S9W$, $S11$, $L15$, $L18W$, and $L24$). The number in the name of each filter corresponds to its effective wavelength. *AKARI*/IRC's nine filters provide us with a unique nine-band photometry continuously covering the whole mid-infrared range (Matsuhara et al. 2006), which makes *AKARI* superior to other infrared telescopes such as *Spitzer* or *WISE* in terms of the wavelength coverage. With this advantage, we are able to analyse the mid-infrared features of low-redshift galaxies more accurately, for example the polycyclic aromatic hydrocarbons (PAH) emission features of star-forming galaxies (e.g. Murata et al. 2014; Kim et al. 2019) or the warm dust emissions from active galactic nuclei (AGN; e.g. Huang et al. 2017; Toba et al. 2020; Wang et al. 2020). Moreover, the *AKARI* NEP data also perform very well in AGN selection based on machine-learning methods (e.g. Poliszczuk et al. 2019; Chen et al. 2021; Poliszczuk et al. 2021). The *AKARI* NEP field has been extensively observed in multiwavelength data (e.g. Kim et al. 2012, 2021; Oi et al. 2014), and many studies in galaxy evolution are expected to be performed with these fruitful data in the future, for example regarding environmental effects on galaxy evolution and AGN activity (Santos et al. submitted).

Although the *AKARI* NEP data are very useful, as previously described, so far only a small number of galaxy clusters have been found in the *AKARI* NEP field. Henry et al. (2006) reported on the *ROSAT* NEP X-ray survey catalogue, and categorized 62 clusters of galaxies. Only seven of them are located in the *AKARI* NEP field. Goto et al. (2008) found 16 galaxy cluster candidates in the *AKARI* NEP deep field (Murata et al. 2013) in 0.5 deg^2 at redshift $0.9 < z < 1.7$ based on a colour-cut method. Ko et al. (2012) reported the discovery of a supercluster at $z = 0.087$ in the NEP. The number of galaxy clusters identified so far is not sufficient for statistical analysis. Also, the clusters' redshifts are not continuously distributed in the whole redshift range, meaning that the study of the evolution of galaxies in clusters (cluster galaxies hereafter) has been limited. Hence, extending the search of galaxy clusters to the entire *AKARI* NEP field in a large redshift range is necessary, and also beneficial for any further studies related to galaxy clusters, such as *Euclid* (Laureijs et al. 2011). Fortunately, an optical survey was conducted on the whole *AKARI* NEP field (Goto et al. 2017) by the Subaru/HSC (Miyazaki et al. 2012), providing deep optical data that can be utilized to search for galaxy clusters.

There are two goals in this study. The first is to provide a catalogue of potential cluster candidates for studying environmental effects in the *AKARI* NEP field with as few requisites as possible. The reason for this is that the number of clusters in the *AKARI* NEP field is limited, so it is undesirable to remove sources because of any assumption or selection, which may reduce the number of potential cluster candidates. By doing so, we can also avoid imposing too

many biases on the clusters, providing a more complete sample for environmental studies. The second is to provide a useful method for finding galaxy clusters, which can be applied to any optical photometric survey. Despite the substantial number of cluster-finding methods available today, there are never too many methods for cluster finding. Different methods have different advantages and disadvantages so are suitable for different situations. Our presented method has the advantage that it is simple and quick, allowing a straightforward operation.

In this paper, we describe our data and method in Section 2. Our results, including galaxy colour, richness, a catalogue and optical images of our cluster candidates, and reliability tests are presented in Section 3. In Section 4, we discuss a comparison with X-ray clusters, a comparison with COSMOS clusters, properties of cluster galaxies, the influence of spectroscopic data, and future prospects. A summary is given in Section 5. Throughout this paper, the cosmology assumed is the following: $H_0 = 70$ km s^{-1} Mpc^{-1}, $\Omega_m = 0.3$, and $\Omega_\Lambda = 0.7$. We use the AB magnitude system unless otherwise noted.

2 DATA AND ANALYSIS

The data and sample selection are described in Section 2.1, while the cluster-finding methods, including the photo-z, density calculation and the friends-of-friends algorithm, are described in Section 2.2.

2.1 Data and sample selection

We used the source catalogue from the HSC survey (Goto et al. 2017; Oi et al. 2021) in the *AKARI* NEP field to detect galaxy clusters using the friends-of-friends algorithm (Huchra & Geller 1982), which requires only the coordinates and the redshifts of galaxies. For the redshifts, we used the following photometric data sets to estimate the photo-z: (1) HSC g, r, i, z, and y bands (Oi et al. 2021), (2) CFHT MegaPrime/MegaCam u band (Huang et al. 2020), and (3) *Spitzer* IRAC 3.6- and 4.5-μm bands (Nayyeri et al. 2018). The data (2) and (3) are included wherever available. Fig. 1 shows the *AKARI* NEP field (red), the HSC observation coverage (grey), the CFHT observation coverage (blue), and the *Spitzer* observation coverage (pink). The crosses represent the positions of cluster candidates (to be discussed in Section 3).

2.1.1 Data

The Subaru HSC data used in this work are described in Oi et al. (2021) and Kim et al. (2021), including the details of the observations and the data reduction. The total exposure times range from 5360 (*i* band) to 27 440 (*g* band) s in each band. The 5σ detection limits of magnitudes for the g, r, i, z, and y bands are 28.6, 27.3, 26.7, 26.0, and 25.6 mag, respectively. There are more than 3 million sources in the original HSC catalogue, and 747 673 sources have 5σ detection in all five HSC bands.

The details of the observations and the data reduction of the u-band data are described in Huang et al. (2020). The CFHT u-band survey observed 3.6 deg^2 in the *AKARI* NEP-Wide field and obtained a total integration time of 4520 to 13 910 s. The u-band data have a 5σ limiting magnitude of 25.4 mag for the whole *AKARI* NEP-Wide field, while they reach 25.8 mag in a deeper 1-deg^2 area. 24 per cent of the HSC 5σ sources are detected in the u-band data.

The *Spitzer* IRAC 3.6- and 4.5-μm-band data come from Nayyeri et al. (2018). The *Spitzer* observations surveyed a 7.04-deg^2 area at NEP, fully covering the *AKARI* NEP field. The 5σ depths of the 3.6-
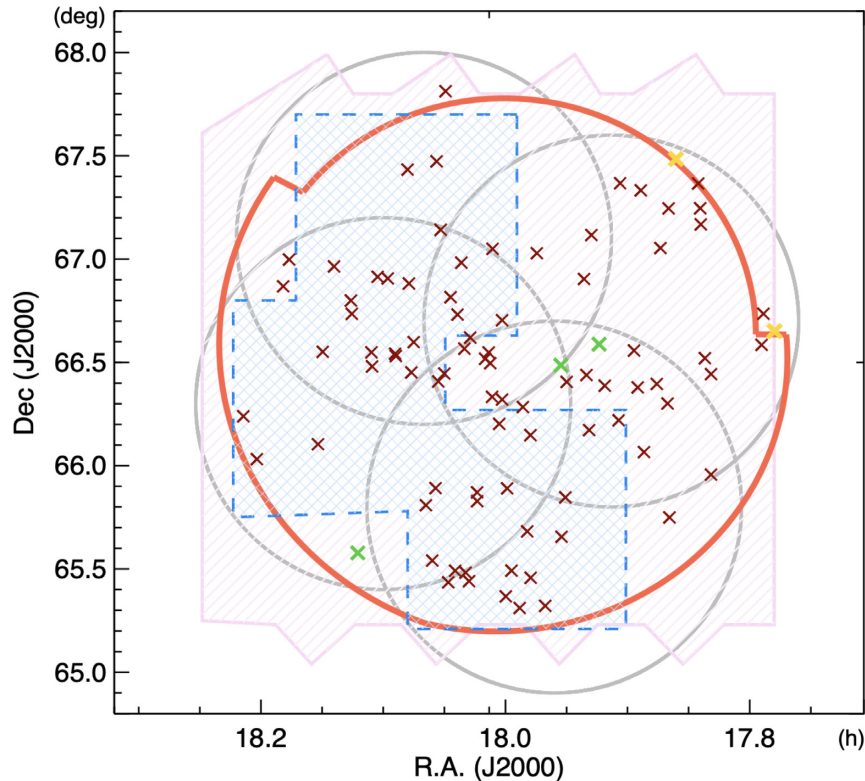
Figure 1. The sky map showing the coverages of the HSC observations (grey), the CFHT observations (blue), and the *Spitzer* observations (pink) in the *AKARI* NEP field (red). The cluster candidates are plotted as crosses, while the candidates matched with X-ray clusters and the candidates near the edge of the HSC survey are plotted in green and orange, respectively.

and 4.5-μm bands are 21.9 and 22.5 mag, respectively. A third of the HSC 5σ sources are observed as the *Spitzer* sources.

The data used for photo-z calculation are summarized in Table 1. In addition, we include 2146 spectroscopic sources at $z \leq 1.1$ to check the photo-z reliability and improve the cluster finding. The distribution of the spectroscopic redshift (spec-z) is plotted in blue in Fig. 2. The spectroscopic data come from various telescopes: MMT/Hectospec and WIYN/Hydra (Shim et al. 2013), GTC/OSIRIS (Díaz Tello et al. 2017), Subaru/FMOS (Oi et al. 2018), Keck/DEIMOS (Takagi et al. 2010; Shogaki et al. 2018; Kim et al. 2018), and *AKARI*/IRC (Ohyama et al. 2018). The approach we used to match the above multiwavelength data is described in Kim et al. (2021).

2.1.2 Sample selection

We required the sources to have 5σ detection in all five HSC bands (i.e., sources fainter than 5σ limiting magnitudes in any HSC band were rejected). An extended/point source classification using the HSC pipeline parameter `base_ClassificationExtendedness_value` was applied to exclude extended sources. A further star–galaxy separation was performed using the χ^2-values from the template fitting (to be discussed in Section 2.2.1) of galaxy (χ^2_{gal}) and star (χ^2_{star}) components: galaxies are selected if $\chi^2_{gal} < \chi^2_{star}$. Because the photo-$z$ performance gets worse at higher redshift, we limited our sample to redshift $z \leq$ 1.1. In total, the HSC sample contains 310 577 sources (we refer to it as the selected sample hereafter). The CFHT u-band data and the *Spitzer*/IRAC data are included with the selected sample to help with the photo-z calculation, if they are available.

2.2 Analysis

2.2.1 Photometric redshift

We used the spectral energy distribution (SED) analysing code LePHARE (Arnouts et al. 1999; Ilbert et al. 2006) to estimate the photo-z (denoted as z_p in equations) of our selected sample. The photo-z distribution is shown in red in Fig. 2. The method of the photo-z calculation is the same as in Ho et al. (2021), but a smaller number of bands are used in this work. In total, a maximum of eight bands (Subaru/HSC g, r, i, z, y, CFHT/Megacam u, *Spitzer*/IRAC 3.6-μm, 4.5-μm) were included in the SED fitting with stellar and galaxy templates. The stellar templates we used were a combination of templates from Bohlin, Colina & Finley (1995), Pickles (1998) and Chabrier et al. (2000). These authors tested several templates for fitting galaxy components, and found that using the COSMOS templates (Ilbert et al. 2009) gave them the most accurate performance in terms of the normalized median absolute deviation (NMAD, σ_{z_p}) and the catastrophic rate (η) for the subset of galaxies with spec-z. The NMAD is defined as $1.48 \times median(\frac{|z_p - z_s|}{1+z_s})$, where z_s denotes the spec-z. The catastrophic rate is defined by the fraction of outliers in the spec-z sample, while an object is regarded as an outlier if $|z_p - z_s|/(1 + z_s) \geq 0.15$. In this work, our photo-z performances are $\sigma_{z_p} = 0.065$ (to be discussed in Sections 2.2.2 and 2.2.3) and $\eta = 8.6$ per cent at $z_p \leq 1.1$ (left-hand panel of Fig. 3). Throughout this work, if a galaxy has the spec-z available then we use that instead. It is noteworthy that the photo-z calculation improves remarkably if we make use of the CFHT and *Spitzer* bands. The right-hand panel of Fig. 3 shows the performance of photo-z calculated by using only five HSC bands, which has a NMAD of 0.074 and an outlier fraction of 19.4 per cent.

Table 1. Summary of the data used for the photo-*z* calculation in this work.

Instrument	Area (deg^2)	Filter	Sensitivity (5σ, AB mag)	Reference
Subaru/HSC	5.4	*g*	28.6	Oi et al. (2021)
	5.4	*r*	27.3	Oi et al. (2021)
	5.4	*i*	26.7	Oi et al. (2021)
	5.4	*z*	26.0	Oi et al. (2021)
	5.4	*y*	25.6	Oi et al. (2021)
CFHT/MegaCam	3.6	*u*	25.4	Huang et al. (2020)
Spitzer/IRAC	7.0	3.6-μm	21.9	Nayyeri et al. (2018)
	7.0	4.5-μm	22.5	Nayyeri et al. (2018)
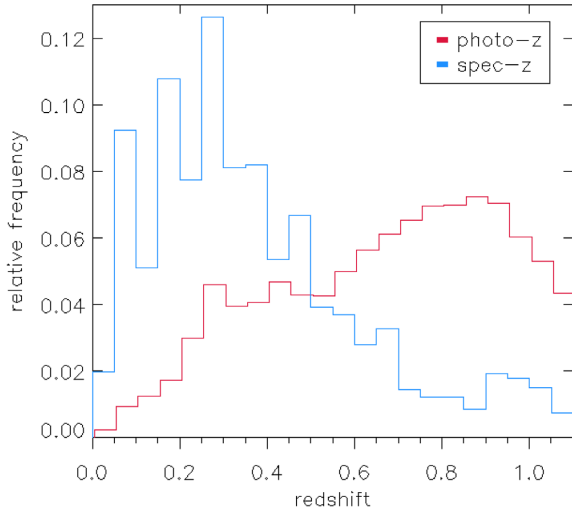
Figure 2. Redshift distributions of the spectroscopic sample of 2146 sources (blue; spec-*z*) and the selected sample of 310 577 sources (red; photo-*z*) from redshift 0 to 1.1. The distribution is plotted in relative frequency; that is, the sum of all bins in each sample is equal to one. The bin size is 0.05.

2.2.2 Local surface density

The 10th-nearest neighbourhood method (e.g. Dressler 1980; Miller et al. 2003) is used to calculate the local density around every galaxy.

Owing to the photo-*z* uncertainty, the local density in this work is calculated in two dimensions within an individual redshift bin of every galaxy: $z \pm \sigma_{z_p} \times (1 + z)$, where $\sigma_{z_p} = 0.065$. We measured the angular separation θ between galaxy pairs as follows:

$$\theta_{1,2} = \cos^{-1}[\sin \delta_1 \sin \delta_2 + \cos \delta_1 \cos \delta_2 \cos (\alpha_1 - \alpha_2)], \quad (1)$$

where $\alpha \in [0, 2\pi]$ and $\delta \in [-\pi/2, \pi/2]$ are right ascension (α) and declination (δ), respectively. Meanwhile, the 10th-nearest local density of each object $\Sigma_{i,10th}$ is simply defined as

$$\Sigma_{i,10th} = \frac{10}{\theta_{i,10th}^2}, \quad (2)$$

where $\theta_{i,10th}$ means the angular separation between the object *i* and its 10th-nearest neighbour within the individual redshift bin.

For sources near the edge of the survey area, the 10th-nearest distance cannot provide the true local density in reality, because some of the neighbouring sources are outside of the survey coverage. Therefore, we performed a correction for the sources that were closer to the edge than to their 10th-nearest neighbours. We assumed that the local densities inside and outside the survey were the same. We drew a circle with its centre at the edge galaxy using the 10th-nearest distance, and measured the area fraction (*x*) outside the survey coverage. We supposed that the *n*th-nearest distance we measured actually was the *m*th-nearest distance in reality (i.e., there are *m* galaxies in the entire circle, while *n* galaxies are located in the survey coverage). As a result of the assumption of uniform density, the
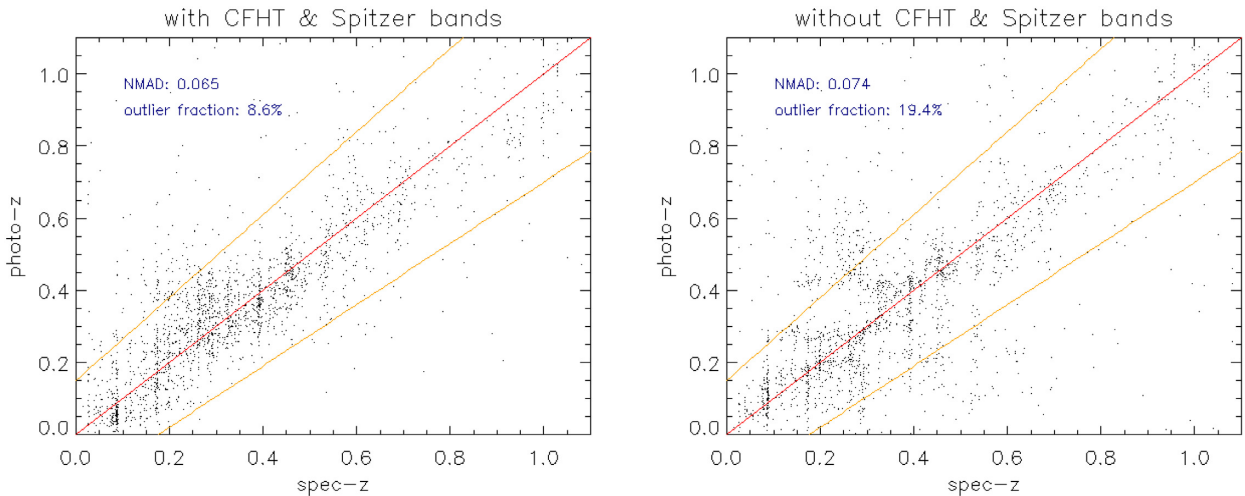
Figure 3. The comparison between photo-*z* and spec-*z* of the spec-*z* sample. The photo-*z* used in this work is plotted in the left-hand panel, while the photo-*z* in the right-hand panel is calculated without the CFHT and *Spitzer* bands. The standard line (i.e. slope equal to one) is plotted in red. The orange lines show where $|z_p - z_s|/(1 + z_s) = 0.15$, which are the borders to define outliers.
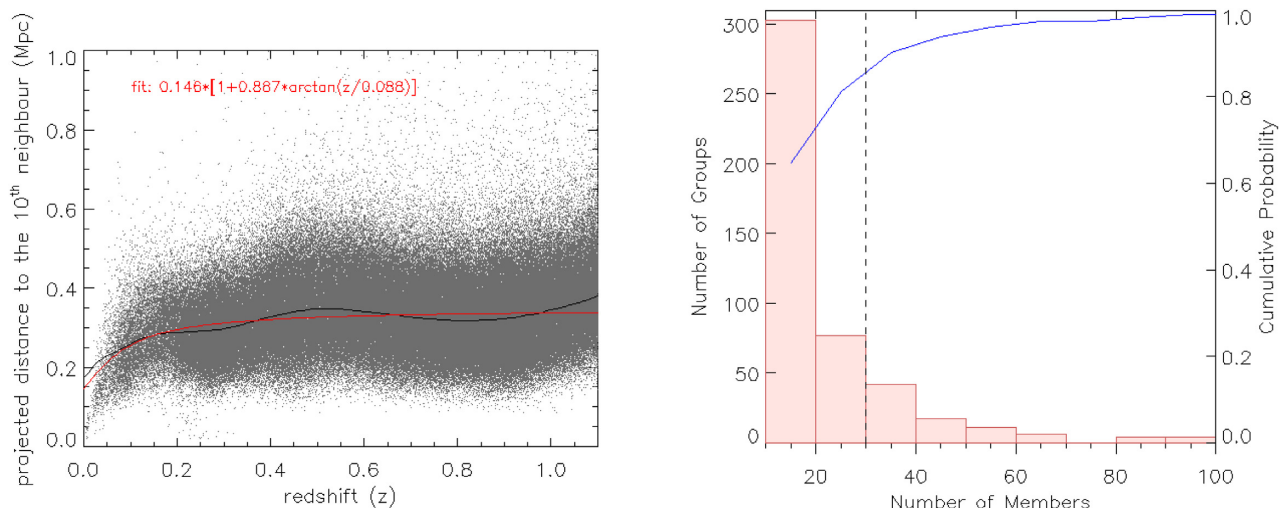
Figure 4. (Left-hand panel) Scatter plot of projected distance to the 10th-nearest neighbour as a function of redshift for every object. Every grey dot represents a galaxy. The black line is the median value of the distance to the 10th-nearest neighbour. The red line is the best-fitting arctangent function to the median values. (Right-hand panel) Histogram of group member numbers. The blue curve shows the cumulative probability. The black line indicates where the member number equals 30, the definition of cluster candidates in this work.

number of galaxies is proportional to the area fraction (x):

$$n : 1 - x = m : 1. \tag{3}$$

Therefore, to obtain the true 10th-nearest distance (i.e. $m = 10$) of the source near the edge, we used the nth-nearest distance instead, where $n = 10(1 - x)$. The n is rounded off to the nearest integer. Note that for some edge sources, their densities do not change after the edge correction, as n is rounded off to 10. Among the 310 577 selected sources, 4732 sources are near the edge, and the corrected local densities are adopted for 3690 sources. More details about the local density calculation and the edge correction are described in Santos et al. (2021 submitted).[1]

We normalized the local density (denoted as Σ^* for the normalized local density) with the median density in the individual redshift bin. There exist 7137 sources (about 2 per cent in the selected sample) with $\Sigma^* > 3$, and 28 498 sources (about 9 per cent in the selected sample) with $\Sigma^* > 2$. We defined those 28 498 objects with $\Sigma^* > 2$ as over-densities. These over-densities were used to search for cluster candidates based on the friends-of-friends algorithm, as described in the next section.

2.2.3 *Friends-of-friends algorithm*

We used the coordinates, defined as the positions of the HSC detections, and the estimated photo-z to select cluster candidates.

We selected cluster candidates by applying the friends-of-friends algorithm to all the over-densities. For each object of the over-densities, its friend is defined if (1) the physical projected distance between them is smaller than a given linking length, and (2) the redshift difference (we call this the linking redshift, Δz, hereafter) between them is smaller than 0.032, which is a half of our photo-z NMAD. This value was chosen empirically. Using a large value such as 0.065 makes the algorithm link galaxies in a wide redshift space, and the redshift of the member galaxies in a generated cluster can

deviate greatly (e.g., $z_{max} - z_{min} > 0.5$), where z_{max} and z_{min} represent the maximum and the minimum redshifts of member galaxies. We reasonably believe that such kinds of results are highly contaminated. We thus adopted a smaller value (half of the photo-z NMAD) as the constraint of the linking redshift in the linking process. Note that we did not make this Δz value redshift-dependent, in order to avoid the wide linking problem described above. We discuss the details of the redshift-dependent linking redshift in Appendix A. Using the value $\Delta z = 0.032$ makes the redshift deviations of cluster galaxies more reasonable. For example, in the worst case of our cluster candidates, $z_{max} - z_{min}$ is about 0.3, which is comparable to the redshift uncertainty $\pm 0.065(1 + z_p)$ at $z_p = 1$.

We used the arctangent function

$$f(z) = d_0 \left[1 + \alpha_0 \arctan (z/z_*) \right] \tag{4}$$

to estimate the linking length, as suggested by Tempel et al. (2014). Three parameters, namely d_0 (in Mpc), α_0, and z_*, were determined by a χ^2-fitting to the median values of the distances to the 10th-nearest neighbours, as shown in Fig. 4. The physical projected distance to the 10th-nearest neighbour of every galaxy is plotted in grey. The median values of the distance to the 10th-nearest neighbour were calculated for 111 redshift bins [$\pm 0.065(1 + z)$, redshift ranges from 0 to 1.1 with a step of 0.01]. The standard errors were applied in the χ^2-fitting. The best-fitting values of the parameters (d_0, α_0, z_*) are (0.146 Mpc, 0.867, 0.088).

We start by looking for friends around the galaxy over-densities using the appropriate linking parameters at the redshift of the over-density. Over-densities with at least 10 friends form an initial group. The friends make other new friends in the same way with their own linking length until no new friends are found. The process ends when all over-densities with at least 10 friends are in a group. The algorithm generated 468 groups in total. The right-hand panel of Fig. 4 presents the numbers of groups for different numbers of galaxy members. There are 165, 88, and 46 groups having more than or equal to 20, 30, and 40 members, corresponding to cumulative relative frequencies of 64.7, 81.2, and 90.2 per cent, respectively. As a compromise between the number of groups and the number of

members, the groups with at least 30 members are defined to be the galaxy cluster candidates.

3 RESULTS

We found 88 cluster candidates in the *AKARI* NEP field (5.4 deg^2) from redshift 0 to 1.1, which are plotted as crosses in Fig. 1 and listed in Table 2 (to be discussed in the following subsections). There are a total of 4390 cluster galaxies. We investigate the colours (Section 3.1) and richness (Section 3.2) of the cluster candidates. The catalogue and optical colour images of the cluster candidates are provided in Sections 3.3 and 3.4, respectively. The reliability of our method and the cluster candidates is examined by false-detection (Section 3.5) and redshift-uncertainty (Section 3.6) tests.

3.1 Colour studies of clusters

We plotted the colour–magnitude diagram ($g - i$ versus i) for every cluster candidate identified in this work. The diagrams of all the candidates are available in the online Supporting Information. Fig. 5 shows the colour–magnitude plots of the X-ray-matched clusters (to be discussed in Section 4.1). The cluster galaxies are plotted with red circles, while grey dots represent the non-cluster galaxies (field galaxies hereafter). Because field galaxies are simply defined as the galaxies not in cluster candidates, this definition includes galaxies in groups with fewer than 30 members. Nevertheless, the number of these group galaxies (5955) is relatively small compared with the number of all field galaxies (306 187), so we believe that the statistical contribution from these group galaxies is negligible. The green line shows the colour cut used to define red galaxies, which is an estimate for the cluster richness in the next Subsection 3.2.

We empirically define that a galaxy is red if its colour is redder than the colour of the $(60 + 30z_{cl})$th percentile in the individual redshift bin $z_{cl} \pm 0.065(1 + z_{cl})$, where z_{cl} is the redshift of the cluster candidate (to be discussed in Section 3.3). Compared with colour cuts for red galaxies from other works, our colour cut is much stricter. For example, Lai et al. (2016) separate red and blue galaxies using $g - i = 1.75$ at $0.6 < z < 0.8$, while our cuts are redder by 0.6 to 0.8 mag in this redshift range. Using their colour cut in our colour–magnitude diagrams (e.g., the right-hand panel of Fig. 5) obviously selects many blue galaxies that do not reside in the galaxy red sequence. We therefore believe that our redshift-dependent colour cut for red galaxy separation is reliable.

3.2 Richness

The cluster richness provides a way to estimate the cluster masses for clusters detected by optical data. We define the richness of our cluster candidates according to the definition from the studies of HSC CAMIRA galaxy clusters (e.g. Murata et al. 2019), that is, the number of red galaxies with stellar mass greater than $10^{10.2} M_\odot$ within $1\ h^{-1}$ Mpc of the cluster centre. Moreover, the mass–richness relationship has been built by the calibration from weak-lensing magnification (Chiu et al. 2020). In this work, the red galaxies are defined by our own definition in Section 3.1, while the stellar mass is calculated based on the best-fitting stellar models from the SED fitting for the photo-z calculation (Section 2.2.1). Fig. 6 shows the density map of cluster candidates in redshift and richness as a contour plot. The plot is generated by 10 bins in the redshift range 0 to 1.1 and richness range 0 to 30, with 10 contour levels.

3.3 Cluster catalogue

We list the cluster candidates in the *AKARI* NEP field in Table 2, including the cluster identifier (ID), cluster number (cl), equatorial coordinates (R.A. and Dec.), cluster redshift (z_{cl}), maximum normalized local density corresponding to each cluster (Σ^*_{max}), number of member galaxies (N), colour cut for red galaxies ($g - i$ cut), number of red galaxies (N_{red}), red galaxy fraction (f_{red}), and cluster richness ($N_{richness}$). The cluster number (cl) is the number generated by our friends-of-friends algorithm for identifying groups. We use this number to discuss cluster candidates throughout this paper for convenience. For instance, the first two cluster candidates in Table 2 are denoted as cl18 and cl9. The coordinates and the redshift of the cluster candidates are defined by the member galaxy with the highest normalized local density. If a cluster has member galaxies detected by a spectroscopic observation, the cluster redshift is defined by spec-z. In some cases (cl1, cl2, cl14, and cl39), the cluster candidates have two or more members with different spec-z. We refer to the spec-z from the brighter/brightest (in the i band) member. Two cluster candidates, cl13 and cl18, have two and one member located near the survey edge, respectively. However, all of their densities remain the same after the edge correction because their edge-corrected n are rounded off to 10, as described in Section 2.2.2. The edge correction does not have a direct impact on the density of our cluster candidates, but overall it affects the normalized density and the galaxy over-density in the cluster-finding process of this work.

3.4 Cluster three-colour images

We obtained colour composite images of the cluster candidates in the *AKARI* NEP field by mosaicking the HSC *g*-, *r*-, and *i*-band images as blue, green, and red using SAOImageDS9 (DS9). We utilized the Subaru HSC coordinates of cluster galaxies to create the input region file of DS9 for the cluster galaxies. The colour optical images of the X-ray-matched clusters (discussed in Section 4) are shown in Fig. 7 as examples. The cluster galaxies are circled in green with a radius of 2 arcsec. The coordinates are shown by cyan dashed lines.

3.5 False detection

We applied our cluster-finding method (i.e. the 10th-nearest neighbour and the friends-of-friends algorithm) to mock galaxy catalogues in order to examine false detection. The mock galaxies were created through the following steps (e.g. Goto et al. 2002; Wen & Han 2021): (1) removing all the cluster galaxies from the selected sample; and (2) shuffling the redshift values in the remaining sample randomly (keeping the same redshift distribution). We repeated the above steps 10 times and generated 10 different mock galaxy catalogues. The clusters generated in this process are regarded as false detections. The number of false detections in every test is shown in Table 3. We obtained the false-detection rate as a function of redshift (Fig. 8) by dividing the false detection number by the number of the true cluster candidates in each redshift bin (0.2 to 0.5, 0.5 to 0.8, and 0.8 to 1.1). The result indicates that about 1 per cent and 4 per cent false detections occur at $z \leq 0.8$ and $z > 0.8$, respectively.

We note that this false-detection test does not take all kinds of possible false detections into account, but simply tests the sensitivity of the whole cluster-finding process to detect chance alignments. Because the groups generated from the friends-of-friends algorithm depend strongly on the linking, there may be unrealized false detections. This could be a significant merging or fragmentation of groups. Thus, we provide a test on the linking length to check

Table 2. Catalogue of the cluster candidates. The columns are ID, cluster number, right ascension, declination, redshift, maximum normalized local density of the member, number of member galaxies, colour cut for red galaxies, number of red galaxies, red galaxy fraction, and cluster richness.

ID	Cl.	R.A.	Dec.	z_{cl}	Σ^*_{max}	N	$g - i$ cut	N_{red}	f_{red}	$N_{richness}$
HSCJ174647+663904[E]	18	266.695	66.6512	0.43	11.30	85	1.90	37	0.44	7
HSCJ174720+664409	9	266.832	66.7359	0.39	9.37	45	1.73	9	0.20	1
HSCJ174725+663506	51	266.854	66.5851	0.63	8.21	47	2.31	28	0.60	18
HSCJ174954+662637	50	267.474	66.4435	0.68	5.11	49	2.40	22	0.45	15
HSCJ174954+655724	68	267.475	65.9566	0.83	9.32	33	2.56	12	0.36	10
HSCJ175012+663115	47	267.550	66.5207	0.73	5.32	51	2.48	34	0.67	22
HSCJ175024+671005	40	267.600	67.1680	0.57	7.64	32	2.24	21	0.66	11
HSCJ175026+671446	19	267.607	67.2460	0.38	4.07	32	1.66	24	0.75	10
HSCJ175032+672156	30	267.632	67.3656	0.49	5.22	41	2.10	28	0.68	12
HSCJ175137+672904[E]	13	267.903	67.4844	0.37	4.98	54	1.65	18	0.33	6
HSCJ175156+654457	76	267.984	65.7491	0.78^s	4.38	52	2.54	9	0.17	8
HSCJ175159+671443	27	267.995	67.2453	0.41	5.38	49	1.83	28	0.57	10
HSCJ175202+661805	7	268.008	66.3014	0.28^s	3.28	30	1.35	6	0.20	0
HSCJ175223+670313	23	268.095	67.0536	0.45^s	8.82	53	2.00	27	0.51	12
HSCJ175234+662346	8	268.140	66.3961	0.32	10.39	44	1.46	13	0.30	2
HSCJ175311+660356	46	268.297	66.0656	0.74	11.64	56	2.50	20	0.36	17
HSCJ175321+671957	66	268.336	67.3326	0.81	4.67	36	2.55	8	0.22	7
HSCJ175330+662245	5	268.374	66.3793	0.28^s	8.99	68	1.34	16	0.24	5
HSCJ175341+663327	38	268.419	66.5576	0.52^s	7.13	131	2.17	52	0.40	26
HSCJ175422+672201	72	268.592	67.3670	0.85	4.59	42	2.57	15	0.36	13
HSCJ175427+661313	59	268.611	66.2202	0.80	4.24	35	2.55	4	0.11	3
HSCJ175508+662315	14	268.782	66.3875	0.39^s	5.05	36	1.74	9	0.25	6
HSCJ175524+663517[X]	29	268.851	66.5881	0.54^s	8.12	64	2.19	45	0.70	25
HSCJ175547+670659	56	268.946	67.1164	0.73^s	9.30	55	2.48	23	0.42	16
HSCJ175554+661022	2	268.974	66.1727	0.19^s	4.02	33	1.21	18	0.55	2
HSCJ175601+662621	39	269.006	66.4392	0.53^s	4.54	47	2.19	16	0.34	8
HSCJ175609+665414	22	269.036	66.9039	0.45	13.34	37	1.98	3	0.08	1
HSCJ175700+662421	3	269.249	66.4058	0.26^s	5.28	55	1.31	26	0.47	1
HSCJ175704+655047	79	269.265	65.8465	0.87	5.77	30	2.58	4	0.13	3
HSCJ175715+653920	12	269.312	65.6556	0.46	3.85	37	2.03	4	0.11	1
HSCJ175717+662912[X]	48	269.320	66.4867	0.69^s	6.61	82	2.41	30	0.37	14
HSCJ175803+651917	11	269.512	65.3213	0.33^s	5.93	47	1.47	15	0.32	4
HSCJ175828+670144	86	269.615	67.0288	0.87	5.26	30	2.58	10	0.33	10
HSCJ175846+652726	24	269.691	65.4572	0.49	8.92	134	2.10	36	0.27	12
HSCJ175846+660853	67	269.693	66.1481	0.87	6.27	41	2.58	3	0.07	2
HSCJ175856+654053	20	269.733	65.6815	0.39^s	3.78	32	1.74	6	0.19	3
HSCJ175909+661703	81	269.786	66.2843	1.00	6.90	36	2.58	2	0.06	2
HSCJ175918+651839	10	269.825	65.3108	0.28^s	5.81	30	1.33	13	0.43	5
HSCJ175942+652929	41	269.926	65.4915	0.65	10.87	95	2.33	37	0.39	23
HSCJ175955+655323	44	269.979	65.8898	0.56	5.45	35	2.23	24	0.69	6
HSCJ175959+652201	16	269.996	65.3670	0.31	6.98	33	1.41	7	0.21	2
HSCJ180010+661915	80	270.041	66.3207	0.80	8.23	42	2.55	4	0.10	4
HSCJ180010+664216	78	270.041	66.7045	0.86	5.95	30	2.58	5	0.17	3
HSCJ180018+661210	49	270.076	66.2027	0.66	5.46	32	2.36	14	0.44	10
HSCJ180038+670300	84	270.158	67.0501	0.91	4.65	31	2.57	4	0.13	2
HSCJ180039+662001	28	270.164	66.3336	0.43	7.10	30	1.93	25	0.83	9
HSCJ180045+662947	69	270.187	66.4964	0.91	4.24	64	2.57	8	0.12	6
HSCJ180049+663254	65	270.206	66.5482	0.78	3.99	35	2.54	6	0.17	5
HSCJ180100+663104	45	270.249	66.5177	0.63	6.00	31	2.31	8	0.26	6
HSCJ180123+654940	15	270.347	65.8279	0.36^s	3.79	32	1.60	9	0.28	1
HSCJ180124+655214	77	270.348	65.8706	0.90	4.90	31	2.57	1	0.03	1
HSCJ180144+663714	58	270.432	66.6205	0.81	11.39	64	2.55	23	0.36	19
HSCJ180147+652627	25	270.447	65.4408	0.42	5.63	44	1.89	21	0.48	9
HSCJ180157+652856	36	270.488	65.4821	0.56	5.52	56	2.22	17	0.30	10
HSCJ180201+663400	52	270.504	66.5667	0.76	8.64	88	2.53	10	0.11	8
HSCJ180210+665859	63	270.541	66.9830	0.82	6.77	32	2.56	2	0.06	1
HSCJ180221+664354	85	270.588	66.7318	0.94	4.02	40	2.57	6	0.15	3
HSCJ180228+652929	55	270.617	65.4914	0.72	4.60	31	2.47	8	0.26	6
HSCJ180242+664858	61	270.673	66.8160	0.85	8.97	84	2.57	20	0.24	17
HSCJ180248+652606	37	270.702	65.4351	0.51	6.49	38	2.13	10	0.26	3
HSCJ180256+674845	35	270.735	67.8124	0.78	7.65	66	2.54	24	0.36	20
HSCJ180300+662646	87	270.750	66.4461	0.96	5.31	31	2.58	2	0.06	2
HSCJ180311+670830	73	270.795	67.1417	1.04	4.63	51	2.62	11	0.22	7

Table 2 – *continued*

ID	Cl.	R.A.	Dec.	z_{cl}	Σ^*_{max}	N	$g-i$ cut	N_{red}	f_{red}	$N_{richness}$
HSCJ180318+662428	83	270.824	66.4079	0.91	5.37	31	2.57	4	0.13	4
HSCJ180323+672822	1	270.845	67.4729	0.17^s	5.06	49	1.19	17	0.35	3
HSCJ180326+655328	17	270.858	65.8910	0.33^s	7.29	180	1.48	106	0.59	49
HSCJ180336+653227	34	270.898	65.5407	0.44	3.90	31	1.94	18	0.58	8
HSCJ180354+654830	21	270.976	65.8082	0.47	12.30	42	2.05	16	0.38	7
HSCJ180430+663555	82	271.126	66.5986	0.85	6.75	30	2.57	3	0.10	2
HSCJ180437+662706	42	271.154	66.4517	0.79	7.96	91	2.54	24	0.26	18
HSCJ180444+665256	32	271.184	66.8821	0.44	8.67	30	1.95	2	0.07	1
HSCJ180448+672559	33	271.201	67.4330	0.53	6.78	34	2.17	6	0.18	2
HSCJ180523+663153	53	271.345	66.5313	0.65	3.43	36	2.34	6	0.17	5
HSCJ180525+663234	62	271.354	66.5427	0.88	8.67	92	2.58	17	0.18	12
HSCJ180547+665424	4	271.444	66.9066	0.29	7.19	94	1.36	20	0.21	4
HSCJ180616+665453	31	271.568	66.9147	0.47	7.06	64	2.04	27	0.42	9
HSCJ180633+662850	70	271.636	66.4806	0.78	7.43	53	2.54	11	0.21	8
HSCJ180635+663256	88	271.644	66.5489	1.07	8.65	39	2.65	3	0.08	2
HSCJ180715+653439^X	6	271.811	65.5774	0.27^s	5.21	45	1.32	28	0.62	2
HSCJ180732+664407	26	271.885	66.7353	0.45	6.34	50	2.00	15	0.30	9
HSCJ180735+664758	64	271.896	66.7995	0.88	9.79	116	2.58	21	0.18	19
HSCJ180825+665753	60	272.103	66.9646	0.77	7.53	45	2.53	5	0.11	4
HSCJ180858+663306	43	272.242	66.5516	0.62	9.10	37	2.29	23	0.62	7
HSCJ180912+660615	75	272.300	66.1041	0.89	4.86	34	2.58	3	0.09	2
HSCJ181037+665952	74	272.654	66.9979	0.87	4.95	31	2.58	5	0.16	4
HSCJ181054+665207	71	272.727	66.8685	0.85	5.47	30	2.57	1	0.03	0
HSCJ181212+660153	57	273.050	66.0313	0.78	12.72	30	2.54	16	0.53	12
HSCJ181252+661422	54	273.216	66.2394	0.87	4.91	39	2.58	7	0.18	5

Notes. ^{s} The cluster has member galaxies detected by spectroscopy, and the redshift is spec-z.
^{X} The cluster is matched with an X-ray cluster.
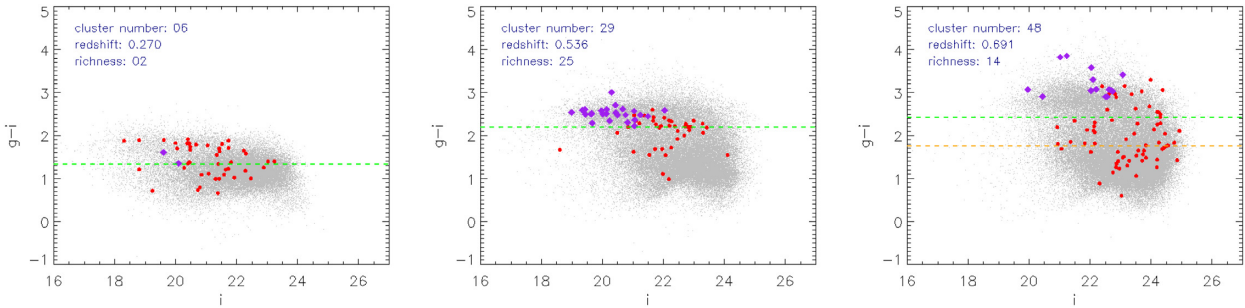^{E} The cluster has member galaxies located near the survey edge.

Figure 5. Colour–magnitude diagrams ($g-i$ versus i) of the X-ray-matched clusters cl6, cl29, and cl48. The red circles are the cluster galaxies, while the grey dots are the field galaxies in the individual redshift bin. The cluster galaxies that contribute to the cluster richness are plotted as purple diamonds. The green dashed line shows the colour cut for red galaxies. For cluster candidates at $0.3 < z < 0.5$ and $0.6 < z < 0.8$, the red galaxy cut defined by Lai et al. (2016) is indicated by the orange dashed line.

that these two cases do not frequently occur during cluster finding, at least in the projected space.

If significant mergers occur, then the number of groups should decrease when a longer linking length is adopted. On the other hand, if significant fragmentations occur owing to a short linking length, then numerous groups will be generated. Fig. 9 shows that the number of groups/clusters generated by our method increases monotonically with the relative linking length from the multiplier of 0.5 to 1.5. This result implies that significant mergers/fragmentations do not commonly occur in the linking in the projected space. We interpret this to mean that our linking length is properly chosen at the intergalactic scale, so that significant mergers at the intercluster scale are avoided. Significant fragmentations are not seen either, as the number of groups drops sharply at a low relative linking length. This is probably a result of the fact that the linking criteria require

10 friends, so that the code does not create overflowing groups with only a few members.

3.6 Redshift-uncertainty test

In this section, we test how redshift uncertainty affects our cluster finding by recovering mock clusters under different NMAD conditions. The mock clusters were generated from our detected cluster candidates by changing the redshift values of them and their member galaxies. We assumed that all the member galaxies in a mock cluster have the same redshift value but diverge with different redshift errors. In a mock cluster, the redshift value is defined to be the mean redshift (z_{mean}) of the detected cluster galaxies. We generated Gaussian-distributed redshift errors (z_{err}) according to given redshift NMAD values (σ_z). The redshift of a mock cluster galaxy in a cluster (z_{mock})
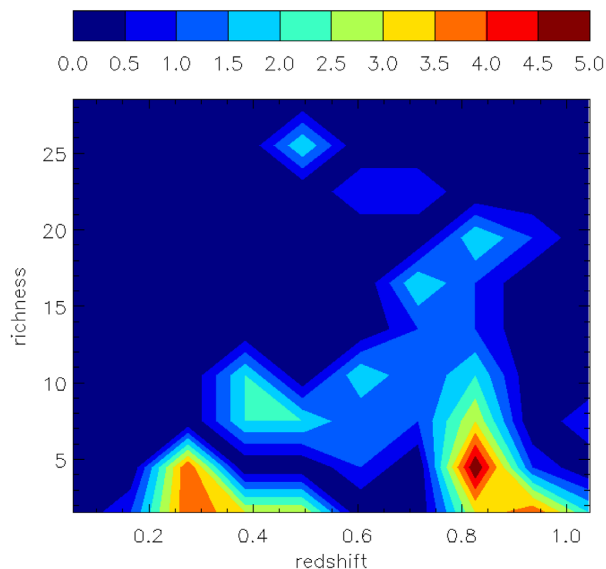
Figure 6. Contour plot presenting the distribution of the cluster candidates in redshift and richness. The contour level is the number density of the cluster candidates.

is written as

$$z_{\rm mock} = z_{\rm mean} + z_{\rm err},$$
$$z_{\rm err} = \sigma_z \left(1 + z_{\rm mean}\right) g(0, 1), \tag{5}$$

where $g(0, 1)$ is a randomly generated number in the Gaussian distribution with a mean of 0 and standard deviation of 1.

We applied our friends-of-friends algorithm to mock cluster catalogues, and then checked the cluster detection to examine the recovery rate of our method. The recovery rate is defined as the number fraction of the recovered clusters. We further categorized the mock clusters into samples in different redshift ranges (0.2 to 0.5, 0.5 to 0.8, and 0.8 to 1.1) and richness ranges (0 to 5, 6 to 14, and larger than or equal to 15). A total of 10 mock cluster samples were created for each redshift/richness range (i.e. 10 tests were performed for each range). To calculate the recovery rate, the average detection was taken, and the errors were estimated by the standard error. Additionally, two redshift NMAD values (0.03 and 0.06) were used to generate the mock clusters for the redshift-uncertainty tests.

The results of the redshift-uncertainty tests are shown in Fig. 10. The triangles and the circles represent the recovery rate from different redshift NMAD values. If the redshift NMAD value is 0.06, which is similar to the photo-z performance of our HSC catalogue used in this work, our method achieves a recovery rate of 45 per cent in the intermediate-redshift range (0.5 to 0.8). The recovery rate drops at high redshifts (>0.8), which could be explained by the high uncertainty (the redshift NMAD is $0.06(1 + z) > 0.1$ as $z > 0.8$). On the other hand, the recovery rate increases with the richness, and reaches 90 per cent in the high-richness sample (larger than or equal to 15).

If the redshift NMAD is 0.03, which is a typical value in higher-quality samples obtained from fields with more photometry such as COSMOS or CFHT Legacy Survey (e.g. Mobasher et al. 2007; Coupon et al. 2009), a 100 per cent recovery rate is achievable for high richness, and it is even possible to have 65 per cent in the most uncertain high-redshift sample ($z>0.8$). The results of the redshift uncertainty analyses imply that our cluster-finding method is feasible, although the current cluster finding is limited by the photo-z accuracy.

4 DISCUSSION

In this section, we discuss the following topics: a comparison with the known clusters detected in the X-ray (Section 4.1); a comparison with the clusters in the COSMOS field (Section 4.2); comparisons between the field and the cluster galaxies (Section 4.3); and cluster finding with the pure photo-z sample (Section 4.4). Finally, we discuss some ongoing and future projects that are planned to perform observations and contribute to cluster studies in the *AKARI* NEP field (Section 4.5).

4.1 X-ray clusters

We compared our cluster candidates with the X-ray clusters detected from *ROSAT* and *Chandra*. The X-ray clusters are listed in Table 4, including the ID, R.A., Dec., redshift, flux, detecting satellite, and match in this work. The *ROSAT* NEP survey (Henry et al. 2006) reported 442 X-ray sources, and among them seven galaxy clusters are located in the *AKARI* NEP field. Two *ROSAT* clusters were recovered by our cluster-finding method (matched with cl6 and cl48). We suspect that the other five *ROSAT* clusters cannot be recovered because they are very near ($z<0.1$), or faint in the X-ray at low redshift ($\sim 5 \times 10^{-14}$ erg cm^{-2} s^{-1} at $z \sim 0.3$). As shown in Fig. 2, our selected sample contains a very limited number of galaxies at $z < 0.1$, because local galaxies are saturated at bright magnitudes in our HSC deep observations. Therefore, intrinsically it is difficult for us to make groups from nearby galaxies and identify nearby clusters. The X-ray luminosity of a cluster is related to its halo mass (e.g. Stanek et al. 2006), so faint clusters may consist of fewer galaxies or have a lower local density, which makes our cluster finding ineffective. On the other hand, two clusters were found in the *Chandra* survey in the *AKARI* NEP field. These two clusters are spatially extended and identified visually in the colour image stacked by three X-ray bands (Krumpe et al. 2015). One of them (cl48) is also detected by *ROSAT* as RXJ1757.3+6631, while the other (cl29) is located around $\alpha=17{:}55{:}12$, $\delta = +66{:}33{:}51$ (hour:minute:second). We simply estimate the flux of the latter unknown *Chandra* cluster in Appendix B. Both of the *Chandra* clusters are recovered through our cluster-finding method. The determination of a match is based on the coordinates and the redshift of the X-ray clusters and our detected cluster candidates. A match is defined if a cluster candidate is close to an X-ray cluster within a 2-arcmin radius and a redshift difference of $0.065(1 + z_{\rm x})$, where $z_{\rm x}$ is the redshift of the X-ray cluster. However, the cluster detected only by *Chandra* has no information in the redshift, so it is based only on the coordinates (matched with cl29). In the case of cl29, 2 arcmin corresponds to 0.7 Mpc at redshift of 0.54, so the matching radius is probably small enough for the claim that the *Chandra* source is correlated with the cluster candidate we found.

4.2 COSMOS clusters

To further ensure the robustness and reliability of our method, we provide a rough examination by applying our cluster finding in the COSMOS photo-z catalogue (Ilbert et al. 2009), which has a photo-z uncertainty of $\sigma_{z_p} = 0.053$ at $0.2 < z < 1.5$, and compare the result with the COSMOS cluster catalogue (Bellagamba et al. 2011).

We mostly adopted the same approach as above, that is, calculating the local density and then grouping by the friends-of-friends algorithm. However, because the photo-z uncertainty and the number density of the COSMOS field are different from those in the *AKARI* NEP field, we determined the linking parameters for the COSMOS field in the same manner as we did for the *AKARI* NEP field. The
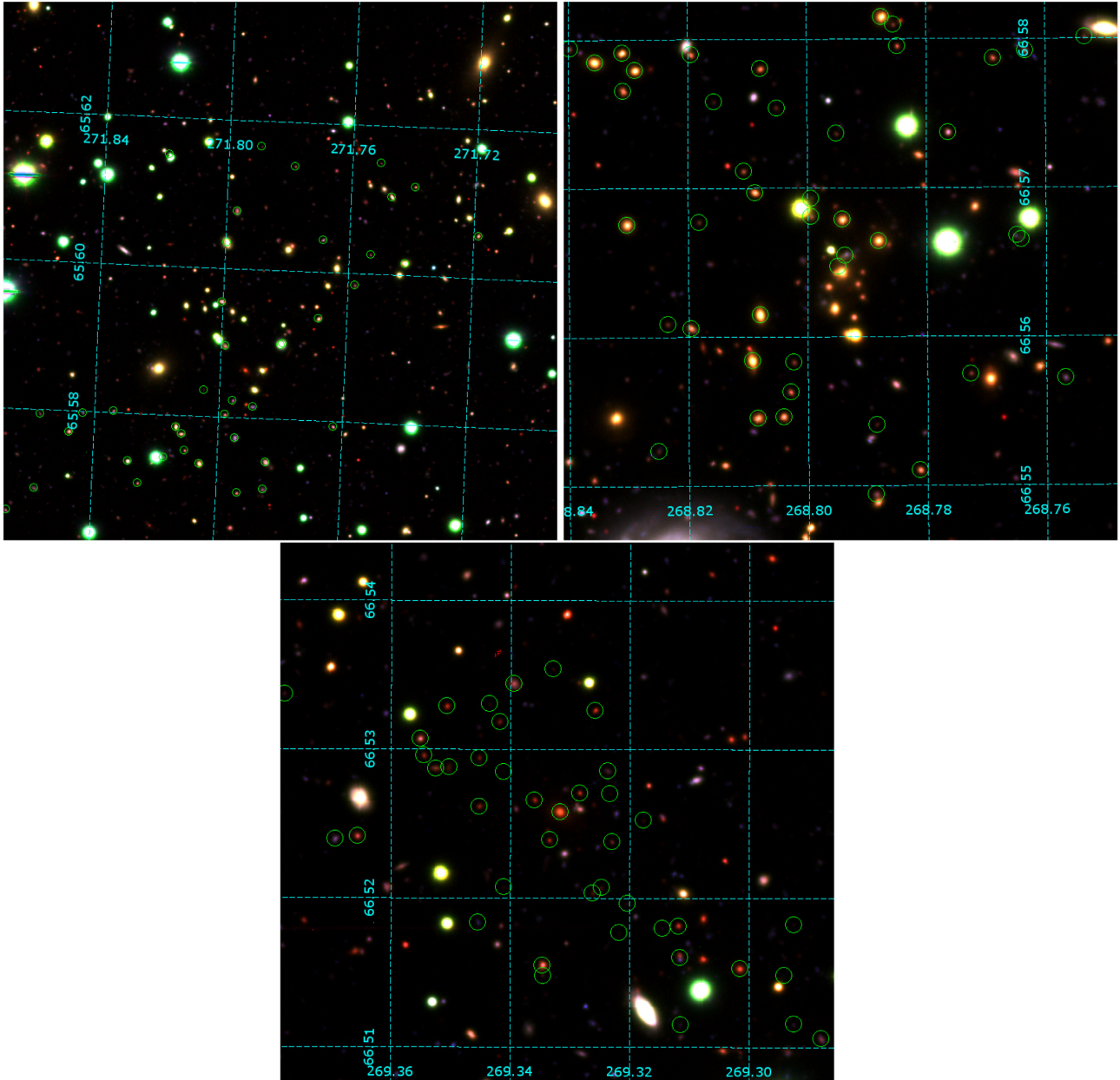
Figure 7. Three-colour images of the X-ray-matched clusters cl6 (upper left), cl29 (upper right), and cl48 (bottom) created by DS9. HSC *g*-, *r*-, and *i*-band images are used as the blue, green, and red colours in the stacking. The cluster galaxies are circled in green, with a radius of 2 arcsec.

Table 3. Number of false detections in every test.

Test	False detection
1	5
2	3
3	1
4	2
5	1
6	4
7	3
8	0
9	0
10	1

individual redshift bin, the linking length, and the linking redshift are determined to be $\pm0.05(1 + z)$, $0.126\,[1 + 2.364\arctan{(z/1.137)}]$ Mpc, and 0.025, respectively. The linking length was obtained by fitting the median projected distance to the 10th-nearest neighbour in Fig. 11.

Our method selected 139 cluster candidates, and 51 of 147 COSMOS clusters are recovered. The match is defined in the same way as in the last section for X-ray clusters. In addition, we used a more relaxed cluster definition of 20 members for comparison in this section. There are 100 additional relaxed cluster candidates, and 20 of them are matched with the COSMOS clusters. The recovery rates as functions of richness and signal-to-noise ratio (S/N), which are provided by the COSMOS cluster catalogue (Bellagamba et al. 2011), are shown in Fig. 12. We also estimated the 'new detection rate' to measure how many cluster candidates are detected by our
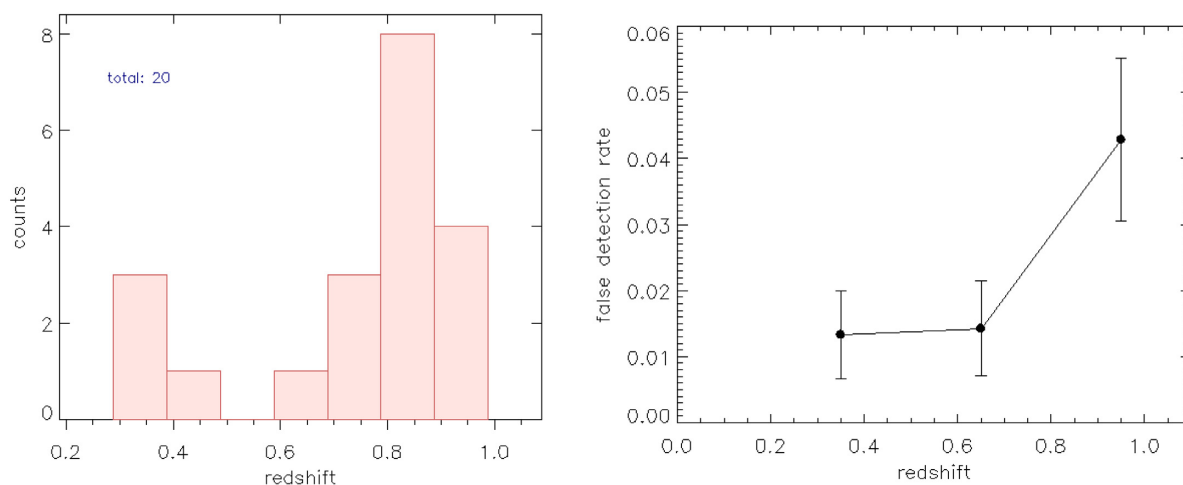
Figure 8. Redshift distribution of the total false detections (left-hand panel, 20 cases from 10 tests) and false-detection rate as a function of redshift (right-hand panel). The errors of the false-detection rate are estimated by the Poisson error.
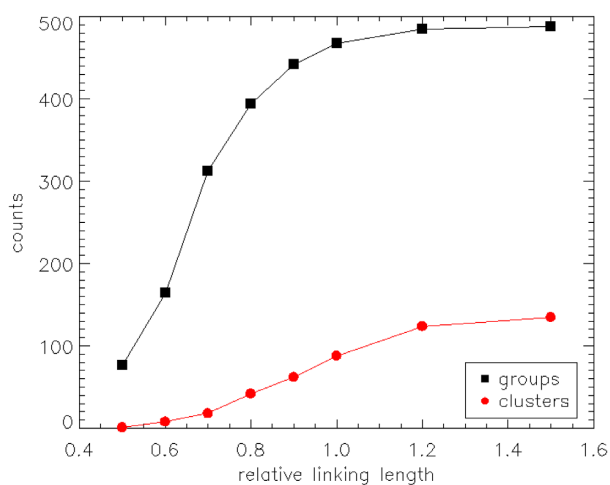
Figure 9. Number of groups (black squares) and clusters (red circles) as functions of the relative linking length, which is given as multiples of the original linking length.

method but not found by COSMOS in Fig. 13. The recovery rate increases with both richness and S/N, which is consistent with the result of the redshift-uncertainty test in Section 3.6 to some extent. Moreover, the low recovery rate at low richness (or low S/N) is relevant to the threshold of member numbers we use to define cluster candidates. Nonetheless, loosening the threshold might be risky, as the 'new detection' increases at the same time . These results may indicate that our method is able to capture high-richness clusters, but has inherent difficulties in detecting low-richness clusters.

4.3 Stellar mass and star-formation rate

In this section, we compare the stellar mass and star-formation rate (SFR) between the cluster galaxies and the field galaxies. Just as for the stellar mass described in Section 3.2, the SFR for every galaxy was also estimated by the SED fitting during the photo-z calculation. Although the SFR is estimated without mid-IR and far-IR photometry, it is still useful for a qualitative comparison of the two galaxy populations. Fig. 14 shows the histogram of the stellar mass and the SFR distributions in different redshift ranges (0.2 to 0.5, 0.5 to 0.8, and 0.8 to 1.1). The field galaxies are plotted in black, while the

cluster galaxies of the cluster candidates with richness greater than 10 are plotted in red. The mean values of the stellar mass and SFR are also shown. The two-sample Z-statistic (Z) is used to measure the difference between the two distributions from the cluster and field galaxy samples:

$$Z = \frac{\overline{X_c} - \overline{X_f}}{\sqrt{\sigma_{X_c}^2 + \sigma_{X_f}^2}}, \tag{6}$$

where $\overline{X_c}$ and $\overline{X_f}$ are the mean values of the stellar mass or SFR for the cluster and the field galaxy sample, respectively. The σ_{X_c} and σ_{X_f} represent the standard errors of the stellar mass or SFR for the cluster and the field galaxy sample, respectively. The results show that the cluster galaxies generally have higher stellar mass and lower SFR compared with field galaxies at $0.2 < z \leq 1.1$ (e.g. Vulcani et al. 2010), while the difference in stellar mass in the highest-redshift bin is not very significant. This indicates that relatively massive cluster galaxies are found by our method. Furthermore, this result may imply that comparing physical properties between cluster and field galaxies statistically using our cluster candidates will be a feasible task in the future.

4.4 Cluster finding without spec-z

In this section, we examine how much the spec-z improves the redshift-based cluster finding by repeating our cluster-finding method with the pure photo-z sample. We found that one original cluster candidate is missed, and two false detection are generated using the pure photo-z sample. The missed cluster candidate is detected as a group with 27 members in the pure photo-z cluster finding, while the two falsely detected cluster candidates are detected as groups with 29 and 26 members in the cluster finding with spec-z. Further comparisons in detection numbers, missing rates, and false-detection rates of the galaxy over-density, groups, and clusters are listed in Table 5. The missing rates and the false-detection rates are defined as $(N_s - N_{int})/N_s$ and $(N_p - N_{int})/N_p$, respectively. Here, N_s, N_p, and N_{int} denote the detection number from including spec-z, the detection number from pure photo-z, and their intersection, respectively. It appears that the results obtained from the pure photo-z catalogue miss the true structures by 1.1 per cent to 1.7 per cent, and have false-detection rates of 1.6 per cent to 3.3 per cent. This may imply that with the aid of a small fraction of spec-z sources
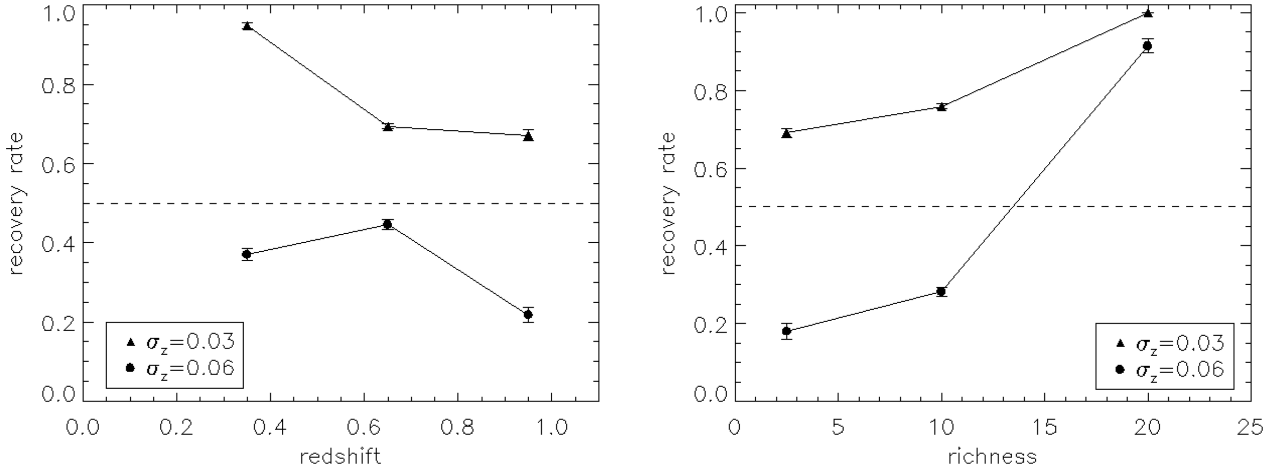
Figure 10. Recovery rate as a function of redshift (left-hand panel) and richness (right-hand panel). The triangles and the circles show the results from the mock cluster sample with different redshift NMAD values, of 0.03 and 0.06, respectively. The errors are estimated by the standard error. The dashed horizontal line indicates the 50 per cent recovery rate.

Table 4. Catalogue of X-ray clusters detected by *ROSAT* and *Chandra* in the *AKARI* NEP field. The columns are ID, right ascension, declination, redshift, flux (0.5 to 2.0 keV), satellite that detected the X-ray cluster, and match with the cluster candidates in this work.

ID	R.A.	Dec.	Redshift	Flux (erg cm^{-2} s^{-1})	Detecting satellite	Match in this work
RXJ1806.8+6537	271.715	+ 65.6294	0.26	2.74×10^{-13}	*ROSAT*	Matched with cl6
RXJ1757.3+6631	269.3325	+ 65.5275	0.69	3.40×10^{-14}	Both	Matched with cl48
RXJ1804.2+6729	271.065	+ 67.4892	0.06	4.99×10^{-14}	*ROSAT*	Not matched
RXJ1754.7+6623	268.6904	+ 66.3981	0.09	1.82×10^{-13}	*ROSAT*	Not matched
RXJ1751.5 6719	267.8788	+ 67.3222	0.09	1.85×10^{-13}	*ROSAT*	Not matched
RXJ1758.9+6520	269.74	+ 65.3494	0.37	3.89×10^{-14}	*ROSAT*	Not matched
RXJ1808.7+6557	272.1817	+ 65.9514	0.25	6.01×10^{-14}	*ROSAT*	Not matched
J175511+663354	268.797	+ 66.565	0.54*	2.94×10^{-14}*	*Chandra*	Matched with cl29

Note. *These values are determined in this work.
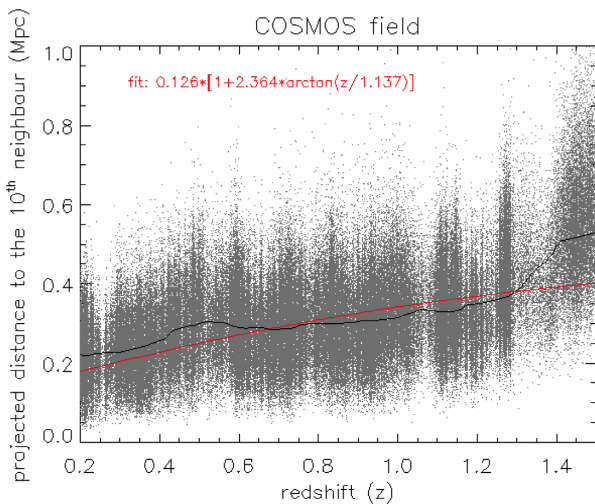
Figure 11. Projected distance to the 10th-nearest neighbour as a function of redshift for the photo-*z* sources in the COSMOS field. The symbols are the same as in the left-hand panel of Fig. 4.

(even less than 1 per cent of the whole selected sample), a marginal improvement in the cluster-finding could be obtained.

4.5 Future prospects

In this section, we describe some large projects for the near future that may help in the study of galaxy clusters in the *AKARI* NEP field. We envision that the cluster candidates provided in this work will be the observation targets in these future projects and will hopefully enhance the chances of finding real clusters. Furthermore, we will be able to confirm how many cluster and cluster galaxy candidates are true with the aid of these follow-up observations, and then we can conduct further cluster studies or improve the cluster finding.

The NEP is one of the major targets of the *Euclid* mission (Laureijs et al. 2011), which also plans to carry out a large-area optical and mid-IR survey for probing galaxy clusters (Euclid Collaboration 2019). The cluster candidates found in this work will be useful as references, and the results of *Euclid* will also help to advance cluster research in the *AKARI* NEP field.

The X-ray detector *eROSITA*, which is expected to carry out an all-sky survey and detect more than 10^5 galaxy clusters (Merloni et al. 2012), has now has been launched and is operational. Having more detected clusters in the *AKARI* NEP field not only directly provides the targets for cluster studies, but also assists the development of cluster-detection programs like this work.

As shown in Sections 3.6 and 4.4, the redshift accuracy is a key variable for our cluster finding. An accurate redshift can only be achieved with a large number of spectroscopic reference objects. Larger spectroscopic surveys on the NEP are planned using the Subaru Prime Focus Spectrograph (PFS; Tamura et al. 2016),
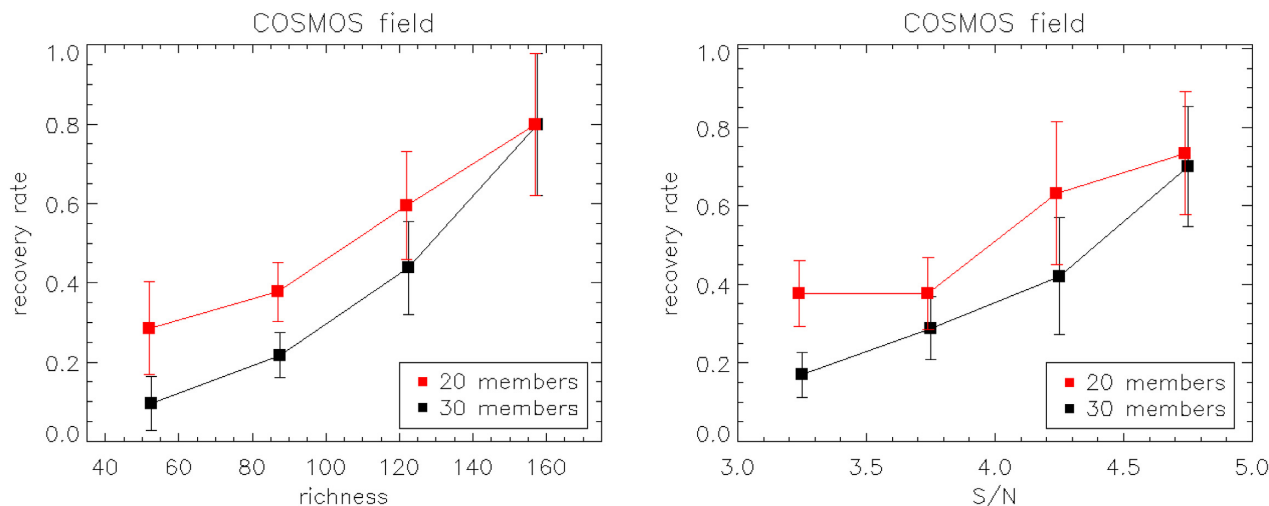
Figure 12. Recovery rate as a function of richness (left-hand panel) and signal-to-noise ratio (right-hand panel) for the COSMOS data. The red and the black squares show the results from the cluster candidates defined by 20 and 30 members, respectively. The errors are estimated by the Poisson error.
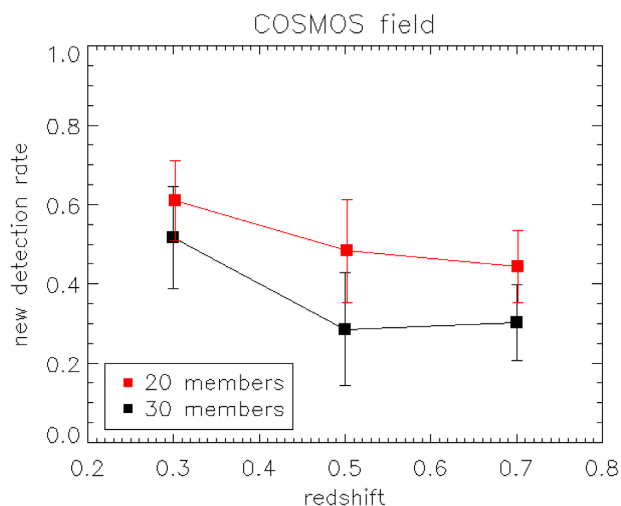

Figure 13. New detection rate as a function of redshift for the COSMOS data. The red and the black squares show the results from the cluster candidates defined by 20 and 30 members, respectively. The errors are estimated by the Poisson error.

which is able to perform spectral observations of 2400 objects simultaneously. Subaru PFS is expected to start operation in 2023. We expect that using Subaru PFS will dramatically increase the sample size of spectroscopic objects in the *AKARI* NEP field in the near future.

TolTEC (Bryan et al. 2018) is a millimetre-wave camera mounted on the focal plane of the 50-m Large Millimeter Telescope (LMT). It is able to provide sensitive three-band imaging at 2.0, 1.4, and 1.1 mm, with a beamsize of 9.5, 6.3, and 5 arcsec, respectively. TolTEC also has fast mapping speed of 69, 20, 12, $\mathrm{deg}^2\,\mathrm{mJy}^{-2}\,\mathrm{h}^{-1}$ at maximum, so it can conduct the 100-deg^2 Large Scale Structure Survey. As one of the main scientific goals of TolTEC, this survey is expected to probe galaxy clusters via the SZ effect using TolTEC's advantageous detectors in its unique three bands.

5 SUMMARY

This work has developed an approach for searching galaxy cluster candidates using only positional information based on the optical detection of galaxies with as few requisites and selection biases as possible. The cluster-finding process applies the friends-of-friends algorithm to galaxy over-densities. The over-densities are selected based on the normalized local surface density of every galaxy determined by the 10th-nearest neighbourhood within individual redshift bins. The linking process of the algorithm is designed to utilize the redshift-dependent linking length and the constant linking redshift. Galaxies having more than 10 friends are made into groups, and groups with 30 or more members are defined to be cluster candidates. All the parameters used in the cluster finding are listed below.

(i) kth-nearest neighbourhood: 10th;
(ii) individual redshift bin: $\pm 0.065(1 + z)$;
(iii) over-density: $>2 \times$ median;
(iv) linking length: $0.146\,[1 + 0.887\arctan(z/0.088)]$ Mpc;
(v) linking redshift: 0.032;
(vi) grouping criterion: 10 friends;
(vii) cluster definition: ≥ 30 members.

As a result, a catalogue of 88 galaxy cluster candidates in the *AKARI* NEP field is presented. Bright X-ray clusters at intermediate redshift can be successfully recovered through our method. The reliability analyses suggest that even under the worst case of the photo-z accuracy, the cluster finding in this work still has a fair performance in the recovery rate of 40 per cent, and a false-detection rate of 1 per cent at redshift 0.2 to 0.8. The cluster candidates with richness greater than or equal to 15 especially have an excellent recovery rate of 90 per cent. Applying our cluster-finding method to the COSMOS field resulted in a recovery of 80 per cent of high-richness and high-S/N clusters. Although some cluster candidates provided in this work might be contaminated by field galaxies, our method is still able to detect some high-confidence cluster galaxy candidates for further studies. The comparison with the pure photo-z sample suggests that having a small fraction of spec-z sources slightly improves the cluster finding. In addition, this method is useful as a first screening for finding galaxy clusters from a large-area survey,
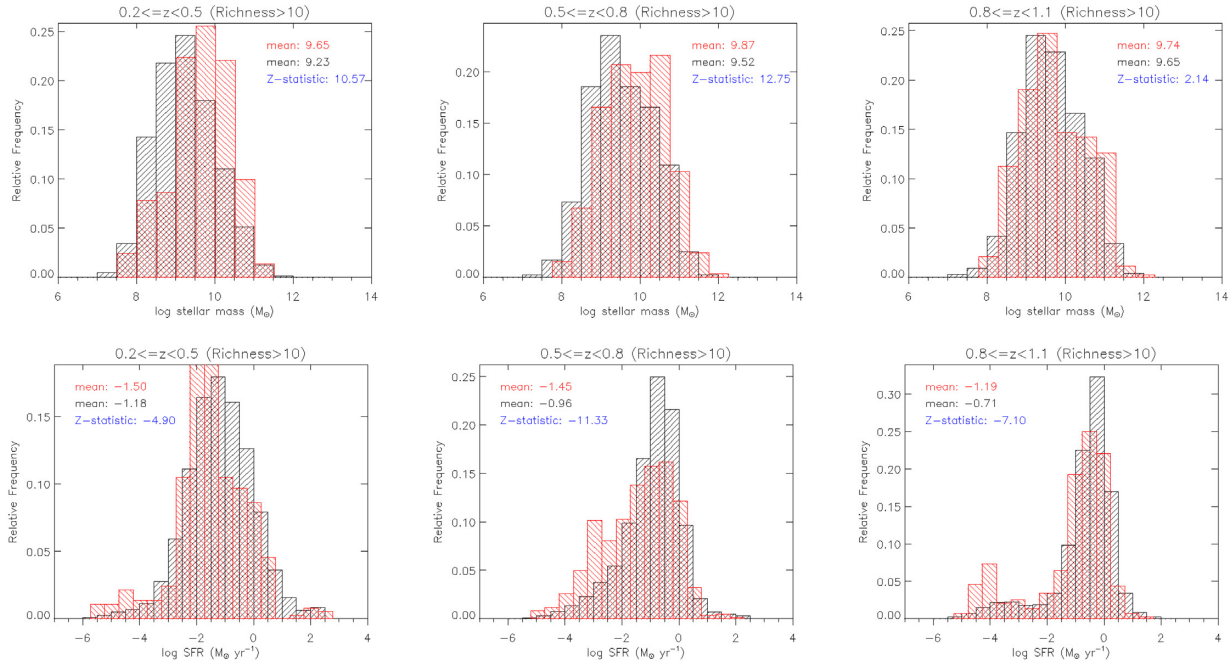
Figure 14. Normalized number distribution of the stellar mass and SFR in log scale. The field galaxies and the cluster galaxies are plotted in black and red, respectively. The mean values of each distribution are shown in corresponding colours.

Table 5. The detection numbers, missing rates, and false-detection rates of galaxy over-densities, groups, group galaxies, clusters, and cluster galaxies. The columns two to four show the detection numbers obtained from the cluster-finding process with spec-z (N_s), with pure photo-z (N_p), and their intersection (N_{int}). The fifth and the sixth columns from the left are the missing rate (($N_s - N_{int}$)/N_s) and the false-detection rate (($N_p - N_{int}$)N_p) of the cluster finding using the pure photo-z catalogue.

	Spec-z (N_s)	Pure photo-z (N_p)	Intersection (N_{int})	Missing rate ($\frac{N_s - N_{int}}{N_s}$) (per cent)	False detection rate ($\frac{N_p - N_{int}}{N_p}$)(per cent)
Over-density	28 498	28 559	28 093	1.4	1.6
Group	468	472	463	1.1	1.9
Group galaxy	10 345	10 446	10 164	1.7	2.7
Cluster	88	89	87	1.1	2.2
Cluster galaxy	4390	4461	4314	1.7	3.3

efficiently providing potential candidates for further X-ray, radio, or any cluster studies. The NEP is a crucial area at which many ongoing or future projects such as *eROSITA* and *Euclid* are aiming. The method and cluster candidates provided by this work will be good references for these projects.

DATA AVAILABILITY

The data underlying this article will be shared on reasonable request to the corresponding author.

REFERENCES

Arnouts S. et al., 1999, MNRAS, 310, 540
Bellagamba F., Maturi M., Hamana T., Meneghetti M., Miyazaki S., Moscardini L., 2011, MNRAS, 413, 1145
Bleem L. E. et al., 2015, ApJ, 216, 27
Bohlin R. C., Colina L., Finley D. S., 1995, AJ, 110, 1316
Böhringer H. et al., 2001, A&A, 369, 826
Bryan S. et al., 2018, Zmuidzinas J., Gao J.-R., eds, Proc. SPIE Conf. Ser. Vol. 10708. p. 107080J, International Society for Optics and Photonics,SPIE, United States, Millimeter, Submillimeter, and Far-Infrared Detectors and Instrumentation for Astronomy IX
Chabrier G., Baraffe I., Allard F., Hauschildt P., 2000, ApJ, 542, 464
Chen B. H. et al., 2021, MNRAS, 501, 3951
Chiu I.-N., Umetsu K., Murata R., Medezinski E., Oguri M., 2020, MNRAS, 495, 428
Coe D., et al, 2013, ApJ, 762, 32
Coupun J., et al, 2009, A&A, 500, 981
Díaz Tello J., et al, 2017, A&A, 604, A14
Dressler A., 1980, ApJ, 236, 351
Ebeling H., Wiedenmann G., 1993, Phys. Rev. E, 47, 704
Euclid Collaboration, 2019, A&A, 627, A23
Fruscione A. et al., 2006, in Silva D. R.,Doxsey R. E., eds,Proc. SPIE Conf. Ser.Vol. 6270. p. International Society for Optics and Photonics,SPIE, United States, 62701V, Observatory Operations: Strategies, Processes, and Systems
Goto T. et al., 2002, AJ, 123, 1807
Goto T., Yamauchi C., Fujita Y., Okamura S., Sekiguchi M., Smail I., Bernardi M., Gomez P. L., 2003, MNRAS, 346, 601
Goto T. et al., 2008, PASJ, 60, S531
Goto T. et al., 2017, Publ. Korean Astron. Soc., 32, 225
Henry J. P. et al., 2006, ApJS, 162, 304
Hilton M. et al., 2020, ApJS, 253, 3
Ho S. C.-C. et al., 2021, MNRAS, 502, 140
Hong T., Han J. L., Wen Z. L., Sun L., Zhan H., 2012, ApJ, 749, 81
Hong T., Han J. L., Wen Z. L., 2016, ApJ, 826, 154
Huang T.-C., Goto T., Hashimoto T., Oi N., Matsuhara H., 2017, MNRAS, 471, 4239
Huang T.-C. et al., 2020, MNRAS, 498, 609
Huchra J. P., Geller M. J., 1982, ApJ, 257, 423
Hung D. et al., 2020, MNRAS, 491, 5524
Hwang H. S., Park C., Choi Y.-Y., 2012, A&A, 538, A15
Ilbert O. et al., 2006, A&A, 457, 841
Ilbert O. et al., 2009, ApJ, 690, 1236
Kim S. J. et al., 2012, A&A, 548, A29
Kim H. K., Malkan M. A., Oi N., Burgarella D., Buat V., Takagi T., Matsuhara H., 2018, in Ootsubo T., Yamamura I., Murata K., Onaka T., eds, The Cosmic Wheel and the Legacy of the AKARI Archive: From Galaxies and Stars to Planets and Life. p. 371,Japan Aerospace Exploration Agency (JAXA),Japan
Kim S. J. et al., 2019, PASJ, 71, 11
Kim S. J. et al., 2021, MNRAS, 500, 4078
Ko J. et al., 2012, ApJ, 745, 181
Komatsu E. et al., 2011, ApJS, 192, 18
Krumpe M. et al., 2015, MNRAS, 446, 911
Lai C.-C. et al., 2016, ApJ, 825, 40
Laureijs R. et al., 2011, Euclid Definition Study Report. preprint (arXiv:1110.3193)
Matsuhara H. et al., 2006, PASJ, 58, 673
Merloni A. et al., 2012, eROSITA Science Book. preprint (arXiv:1209.3114)
Miller C. J., Nichol R. C., Gómez P. L., Hopkins A. M., Bernardi M., 2003, ApJ, 597, 142
Miyazaki S. et al., 2012, McLean I. S., Ramsay S. K., Takami H., eds, Proc. SPIE Conf. Ser.Vol. 8446. p. 84460Z
Mobasher B. et al., 2007, ApJS, 172, 117
Murakami H. et al., 2007, PASJ, 59, S369
Murata K. et al., 2013, A&A, 559, A132
Murata K. et al., 2014, A&A, 566, A136
Murata R. et al., 2019, PASJ, 71, 107
Muzzin A., Wilson G., Demarco R., Lidman C., Nantais J., Hoekstra H., Yee H. K. C., Rettura A., 2013, ApJ, 767, 39
Nayyeri H. et al., 2018, ApJ, 234, 38
Oguri M. et al., 2018, PASJ, 70, S20
Ohyama Y. et al., 2018, A&A, 618, A101
Oi N. et al., 2014, A&A, 566, A60
Oi N., Goto T., Malkan M. A., Pearson C., Matsuhara H., 2018, PASJ, 69, 70
Oi N. et al., 2021, MNRAS, 500, 5024
Onaka T. et al., 2007, PASJ, 59, S401
Park C., Hwang H. S., 2009, ApJ, 699, 1595
Pickles A. J., 1998, PASP, 110, 863
Planck Collaboration XXIX, 2014, A&A, 571, A29
Planck Collaboration XXVII, 2016, A&A, 594, A27
Poliszczuk A. et al., 2019, PASJ, 71, 65
Poliszczuk A. et al., 2021, A&A, 651,A108
Rykoff E. S. et al., 2014, ApJ, 785, 104
Shim H. et al., 2013, ApJS, 207, 37
Shogaki A. et al., 2018, in Ootsubo T., Yamamura I., Murata K., Onaka T., eds, The Cosmic Wheel and the Legacy of the AKARI Archive: From Galaxies and Stars to Planets and Life. p. 367W, Japan Aerospace Exploration Agency (JAXA), Japan
Stanek R., Evrard A. E., Böhringer H., Schuecker P., Nord B., 2006, ApJ, 648, 956
Staniszewski Z. et al., 2009, ApJ, 701, 32
Sunyaev R. A., Zeldovich Y. B., 1980, ARA&A, 18, 537
Takagi T. et al., 2010, A&A, 514, A5
Takey A., Schwope A., Lamer G., 2011, A&A, 534, A120
Tamura N. et al., 2016, Evans C. J., Simard L., Takami H., eds, Proc. SPIE Conf. Ser. Vol. 9908. p. 99081M, International Society for Optics and Photonics,SPIE, United Kingdom, Ground-based and Airborne Instrumentation for Astronomy VI
Tempel E. et al., 2014, A&A, 566, A1
Toba Y. et al., 2020, ApJ, 899, 35
Vulcani B. et al., 2010, ApJ, 710, L1
Wang T.-W. et al., 2020, MNRAS, 499, 4068
Wen Z. L., Han J. L., 2021, MNRAS, 500, 1003
Wen Z. L., Han J. L., Liu F. S., 2012, ApJS, 199, 34

SUPPORTING INFORMATION

Supplementary data are available at *MNRAS* online.

Please note: Oxford University Press is not responsible for the content or functionality of any supporting materials supplied by the authors. Any queries (other than missing material) should be directed to the corresponding author for the article.

APPENDIX A: LINKING REDSHIFT

In this section, we discuss the usage of the redshift-dependent linking redshift.

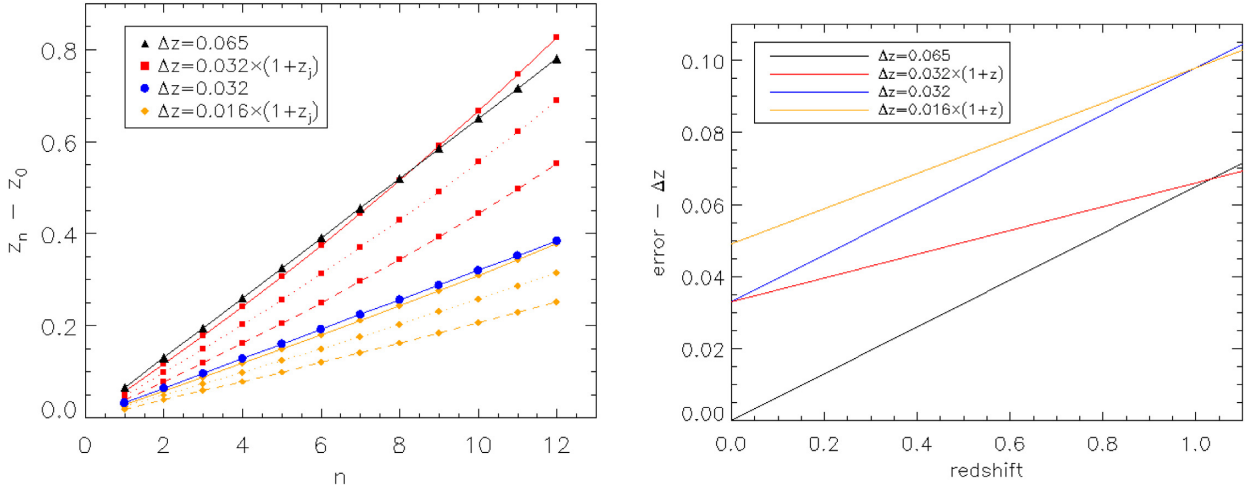$$\Delta z = \Delta s \times (1 + z), \qquad (A1)$$

Figure A1. (Left-hand panel) Relationships between the maximum redshift difference generated from the linking process and the linking times for different linking redshifts Δz. The dashed, dotted, and solid lines represent the initial redshifts $z_0 = 0.2$, 0.5, and 0.8, respectively. (Right-hand panel) Difference between the photo-z error, $0.065(1 + z)$, and different Δz as a function of redshift.

where Δs is a constant value we choose for the linking process. Then after linking j times, the redshift z_j that the linking process can extend in the most extreme case is described in a recurrence relationship:

$$z_j = z_{j-1} + \Delta s \times (1 + z_{j-1}). \tag{A2}$$

We solve this equation by adding 1 to both sides and then making products from $j = 1$ to $j = n$ to obtain

$$1 + z_n = (1 + \Delta s)^n (1 + z_0). \tag{A3}$$

We plot the relationship between the maximum redshift difference $z_n - z_0$ and the linking times n in the left-hand panel of Fig. A1. We plot the relationships of constant linking redshift $\Delta z = 0.065$ and $\Delta z = 0.032$ in black triangles and blue circles. For the redshift-dependent linking redshift, the relationship depends on the initial redshift z_0, and thus multiple curves of $z_0 = 0.2$, 0.5, and 0.8 are plotted, with dashed, dotted, and solid lines, respectively. The red squares and the orange diamonds show the relationships of $\Delta z = 0.032 (1 + z_j)$ and $\Delta z = 0.016 (1 + z_j)$. We compare the constant linking redshift $\Delta z = 0.032$ used in this work with the redshift-dependent linking redshift $\Delta z = 0.032 (1 + z_j)$. For the redshift-dependent one, an initial galaxy at redshift 0.5 ($z_0 = 0.5$) can be grouped with a galaxy at redshift 1.06 ($z_{10} = 1.06$) after linking 10 times ($n = 10$), while the linking with the constant value gives a deviation of 0.32 in this situation. Using the redshift-dependent linking redshift with a smaller Δs can solve the wide linking problem. However, another issue arises, namely that the difference between our photo-z error, $0.065 (1 + z)$, and the linking redshift becomes larger with smaller Δs, especially at low redshift (right-hand panel of Fig. A1). To summarize, according to this study we may not be able to claim which linking redshift is better,

but at least there is no obvious benefit to using a redshift-dependent one.

APPENDIX B: FLUX ESTIMATION OF THE *CHANDRA* CLUSTER J175511+663354

We obtained the observed image (Krumpe et al. 2015) around the *Chandra* cluster from Stacking Analysis of *Chandra* Images (CSTACK[2]) developed by Takamitsu Miyaji. We detected the source of the cluster using VTPDETECT (Ebeling and Wiedenmann 1993) in *Chandra* Interactive Analysis of Observations (CIAO; Fruscione et al. 2006). We set the scale parameter of VTPDETECT to be 0.15, so that faint sources like clusters can be detected (Fig. B1). The X-ray flux was estimated by Portable Interactive Multi-Mission Simulator (PIMMS[3]). The input parameters are listed in Table B1. The estimated flux of the *Chandra* cluster in 0.5 to 2.0 keV is 2.937×10^{-14} erg cm^{-2} s^{-1}.

[1]*Department of Space and Astronautical Science, Graduate University for Advanced Studies, SOKENDAI, Shonankokusaimura, Hayama, Miura District, Kanagawa 240-0193, Japan*
[2]*Institute of Space and Astronautical Science, Japan Aerospace Exploration Agency, 3-1-1 Yoshinodai, Chuo-ku, Sagamihara, Kanagawa 252-5210, Japan*
[3]*Institute of Astronomy, National Tsing Hua University, No. 101, Section 2, Kuang-Fu Road, Hsinchu City 30013, Taiwan*
[4]*Centre for Informatics and Computation in Astronomy (CICA), National Tsing Hua University, 101, Section 2, Kuang-Fu Road, Hsinchu City 30013, Taiwan*

[2]http://lambic.astrosen.unam.mx/cstack/
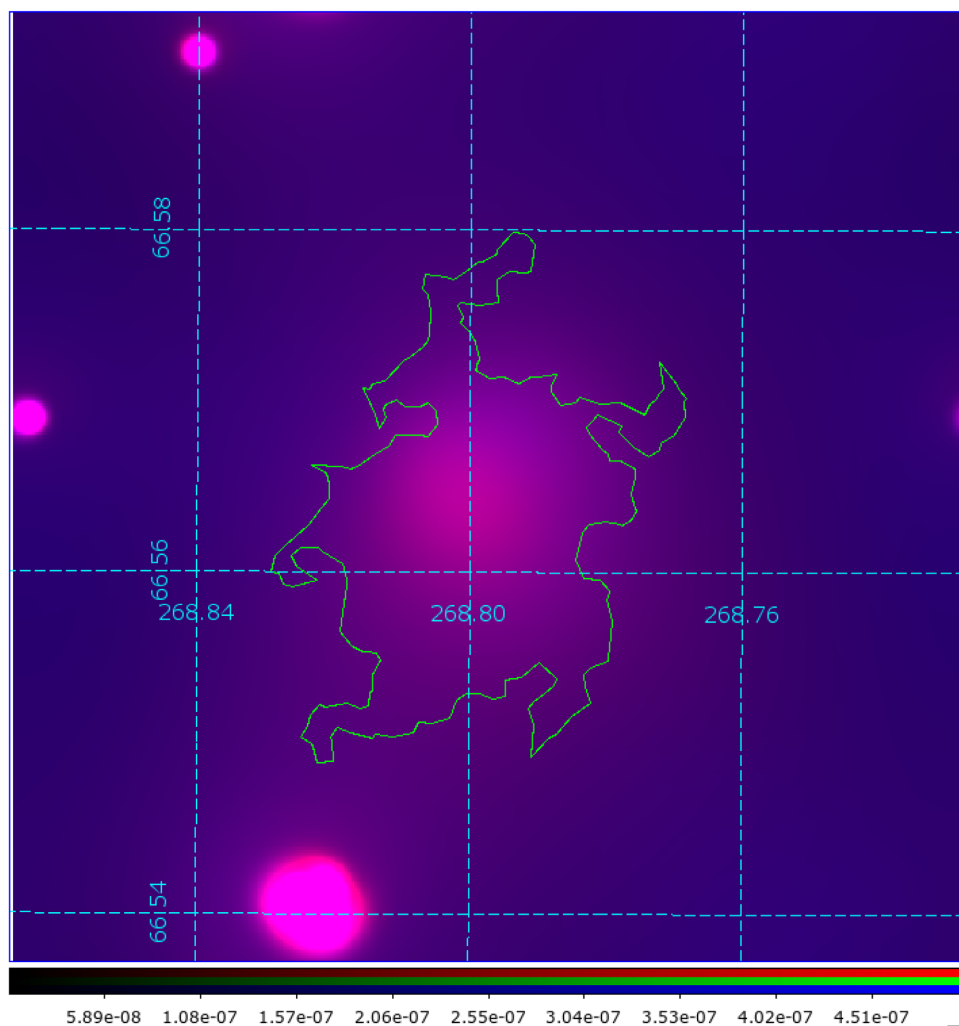[3]https://cxc.harvard.edu/toolkit/pimms.jsp

Figure B1. Smoothed *Chandra* image of the cluster J175511+663354. The image is stacked by images in two bands (0.5 to 2.0 keV in red, and 2.0 to 8.0 keV in blue). The green polygon covers the source region detected by VTPDETECT with the parameter scale = 0.15. The coordinates are plotted with cyan dashed lines. The number in the colour scale bar is the count rate (in counts s^{-1}), while the green colour in this scale bar is not used in this figure.

Table B1. Input parameters for the flux estimation of the *Chandra* cluster J175511+663354 using PIMMS. The NH stands for the column density of hydrogen atoms.

Parameter	Value
Mission	CHANDRA-Cycle 12
Detector	ACIS-I
Grating	None
Filter	None
Input energy	0.5 to 2.0 keV
Model	Plasma/APEC
Galactic NH	4×10^{20} cm^{-2}
Redshift	0.5
Redshifted NH	0
Abundance	0.2 solar
log T (keV)	7.55	3.0575

[5]*National Astronomical Observatory of Japan, 2-21-1 Osawa, Mitaka, Tokyo 181-8588, Japan*

[6]*National Institute of Technology, Wakayama College, 77 Noshima, Nada-cho, Gobo, Wakayama 644-0023, Japan*

[7]*Tokyo University of Science, 1-3 Kagurazaka, Shinjuku-ku, Tokyo 162-8601, Japan*

[8]*Department of Physics and Astronomy, UCLA, 475 Portola Plaza, Los Angeles, CA 90095-1547, USA*

[9]*National Centre for Nuclear Research, ul. Pasteura 7, 02-093 Warsaw, Poland*

[10]*Astronomical Observatory of the Jagiellonian University, ul. Orla 171, 30-244 Cracow, Poland*

[11]*School of Physical Sciences, The Open University, Milton Keynes MK7 6AA, UK*

[12]*Department of Earth Science Education, Kyungpook National University, 80 Daehak-ro, Buk-gu, Daegu 41566, Republic of Korea*

[13]*Instituto de Astronomía, Universidad Nacional Autónoma de México (UNAM), AP 106, Ensenada 22860, BC, Mexico*

[14]*Leibniz Institut für Astrophysik Potsdam (AIP), An der Sternwarte, Potsdam 14482, Germany*

[15]*Astronomy Program, Department of Physics and Astronomy, Seoul National University, 1 Gwanak-ro, Gwanak-gu, Seoul 08826, Republic of Korea*

[16]*Department of Physics and Astronomy, University College London, Gower Street, London WC1E 6BT, UK*

[17]*Cosmic Dawn Center (DAWN), DTU Space, Elektrovej 327, 2800 Kgs. Lyngby, Copenhagen, Denmark*

[18]*National Space Institute, DTU Space, Technical University of Denmark, Elektrovej 327, DK-2800 Kgs. Lyngby, Denmark*

[19]*RAL Space, Rutherford Appleton Laboratory, Chilton, Didcot OX11 0QX, UK*

[20]*Oxford Astrophysics, University of Oxford, Keble Rd, Oxford OX1 3RH, UK*

[21]*Department of Astronomy, Kyoto University, Kitashirakawa-Oiwake-cho, Sakyo-ku, Kyoto 606-8502, Japan*

[22]*Academia Sinica Institute of Astronomy and Astrophysics, 11F of Astronomy-Mathematics Building, AS/NTU, No. 1, Section 4, Roosevelt Road, Taipei 10617, Taiwan*

[23]*Research Center for Space and Cosmic Evolution, Ehime University, 2-5 Bunkyo-cho, Matsuyama, Ehime 790-8577, Japan*

[24]*Niels Bohr Institute, University of Copenhagen, Lyngbyvej 2, 2100 Copenhagen, Denmark*

[25]*Korea Astronomy and Space Science Institute (KASI), 776 Daedeok-daero, Yuseong-gu, Daejeon 34055, Republic of Korea*

[26]*Department of Physics, National Chung Hsing University, 145 Xingda Rd., South Dist., Taichung 40227, Taiwan*

[27]*SNU Astronomy Research Center, Seoul National University, 1 Gwanak-ro, Gwanak-gu, Seoul 08826, Republic of Korea*

This paper has been typeset from a TEX/LATEX file prepared by the author.